Summertime observations of elevated levels of ultrafine particles in the high Arctic marine boundary layer

Julia Burkart[1], Megan D. Willis[1], Heiko Bozem[2], Jennie L. Thomas[3], Kathy Law[3], Peter Hoor[2], Amir A. Aliabadi[4], Franziska Köllner[5], Johannes Schneider[5], Andreas Herber[6], Jonathan P. D. Abbatt[1], W. Richard Leaitch[7].

[1] {Department of Chemistry, University of Toronto, Toronto, Canada}

[2] {Institute of Atmospheric Physics, Johannes Gutenberg-University, Mainz, Germany}

[3] {LATMOS/IPSL, UPMC Univ. Paris 06 Sorbonne Universités, UVSQ, CNRS, Paris, France}

[4] {Environmental Engineering Program, University of Guelph, Guelph, Canada}

[5] {Particle Chemistry Department, Max Planck Institute for Chemistry, Mainz, Germany}

[6] {Alfred Wegener Institute, Helmholtz Center for Polar and Marine Research, Bremerhaven, Germany}

[7] {Environment and Climate Change Canada, Toronto, Ontario, Canada}

Correspondence to: J. Burkart (jburkart@chem.utoronto.ca)

Abstract

Motivated by increasing levels of open ocean in the Arctic summer and the lack of prior altitude-resolved studies, extensive aerosol measurements were made during 11 flights of the NETCARE July 2014 airborne campaign from Resolute Bay, Nunavut. Flights included vertical profiles (60 to 3000 m above ground level) over open ocean, fast ice, and boundary layer clouds and fogs. A general conclusion, from observations of particle numbers between 5 and 20 nm in diameter ($N_{5\text{-}20}$), is that ultrafine particle formation occurs readily in the Canadian high Arctic marine boundary layer, especially just above ocean and clouds, reaching values of a few

thousand particles/cm^3. By contrast ultrafine particle concentrations are very much lower in the free troposphere. Elevated levels of larger particles (for example, from 20 to 40 nm in size, N_{20-40}) are sometimes associated with high N_{5-20}, especially over low clouds, suggestive of aerosol growth. The number densities of particles greater than 40 nm in diameter ($N_{>40}$) are relatively depleted at the lowest altitudes, indicative of depositional processes that will lower the condensation sink and promote new particle formation. The number of cloud condensation nuclei (CCN, measured at 0.6% supersaturation) are positively correlated with the numbers of small particles (down to roughly 30 nm), indicating that some fraction of these newly formed particles are capable of being involved in cloud activation. Given that the summertime marine Arctic is a biologically active region, it is important to better establish the links between emissions from the ocean and the formation and growth of ultrafine particles within this rapidly changing environment.

1 Introduction

Surface temperatures within the Arctic are rising almost twice as fast as in any other region of the world. As a manifestation of this rapid change the summer sea ice extent has been retreating dramatically over the past decades with the possibility that the Arctic might be ice free by the end of this century (Boé et al., 2009) or even earlier (Wang and Overland, 2012). Arctic aerosol is well known to show a distinct seasonal variation with maximum mass concentrations and a strong long-range anthropogenic influence in winter and early spring. The phenomenon, known as Arctic Haze, was identified many years ago (e.g. Barrie, 1986; Heintzenberg, 1980; Rahn et al., 1977; Shaw, 1995), and has commanded renewed attention in recent years (e.g. Law et al., 2014; Quinn et al., 2007). During summer the Arctic is more isolated from remote anthropogenic sources and represents a comparatively pristine environment. The reason is that the Arctic front (e.g. Barrie, 1986), which provides a meteorological barrier for lower-level air mass exchange, moves north of many source regions during the summer months. Anthropogenic and biomass burning aerosols are transported to the Arctic during the summer, but increased aerosol scavenging helps maintain the pristine conditions near the surface (e.g. Browse et al., 2012; Croft et al., 2016a; Garrett et al., 2011).

Zhang et al. (2010) discuss the impacts of declining sea ice on the marine planktonic ecosystem, which includes increasing emissions of dimethyl sulfide (DMS) that may contribute to particle formation in the atmosphere (e.g. Charlson et al., 1987; Pirjola et al., 2000). Enhanced secondary organic aerosol from emissions of biogenic volatile organic compounds is also a possibility (Fu et al., 2009). Primary emissions of aerosol particles from the ocean, such as sea salt and marine primary organic aerosol, may also increase (Browse et al., 2014). Open water tends to increase cloudiness, which means that aerosol influences on clouds are likely to be more important. Over the Arctic the effects of aerosols on clouds are especially uncertain. Models have predicted that increasing numbers of particles may lead to overall warming (Garrett, 2004) when the atmosphere exists in a particularly low particle number state now referred to being "CCN limited" (Mauritsen et al., 2011), to an overall cooling effect when increasing numbers of particles are added to an atmosphere with more particles already present (Lohmann and Feichter, 2005; Twomey, 1974). It is important to characterize particle size distributions in this pristine environment to provide a baseline against which future measurements can be compared in a warming world. Indeed, Carslaw et al. (2013) highlight the need to understand pre-industrial-like environments with only natural aerosols in order to reduce the uncertainty in estimations of the anthropogenic aerosol radiative forcing.

Primary sources, gas-to-particle formation processes, cloud processing, atmospheric aging, mixing and deposition are all reflected in the size distribution. Therefore, measurements of aerosol size distributions are important for understanding the processes particles undergo in addition to their potential effects on clouds. The presence of ultrafine particles indicates recent production as their lifetime is on the order of hours. We focus this paper on ultrafine particles as these are an indication for in-situ aerosol production processes in the Arctic. We also consider the growth of newly formed particles, as that determines how important they are for climate.

Aerosol size distributions including ultrafine particles ($dp < 20$ nm) have been measured before at different locations throughout the Arctic. Long term studies at ground stations such as Alert, Nunavut (Leaitch et al., 2013), Ny Alesund and Zeppelin (Engvall et al., 2007; Ström et al., 2003, 2009; Tunved et al., 2013), both on Svalbard and very recently in Tiksi, Russia (Asmi et al., 2016) and Station Nord, Greenland (Nguyen et al., 2016) indicate a strong seasonal

dependence of the size distribution with the accumulation mode aerosol dominating during the winter months and a shift to smaller particles during the summer months. New particle formation events are frequently observed from June to August. Ström et al. (2003) show that the size distribution undergoes a rapid change from an accumulation mode dominated distribution during the winter months to an Aitken mode dominated distribution at the beginning of summer. Total number concentrations increase at the beginning of summer and roughly follow the incoming solar radiation on a seasonal scale suggesting that photochemistry is an important factor for new particle formation in the Arctic. At Ny Alesund maximum number concentrations occur in late summer and are explained by the Siberian tundra being a potential source of aerosol precursor gases (Ström et al., 2003) and marine biogenic sulphur (Heintzenberg and Leck, 1994). Analysis of air mass patterns for this region show that the shift in the size distributions is also accompanied by a change of source areas, with a dominance of Eurasian source areas in winter and North Atlantic air during summer (Tunved et al., 2013).

Particle measurements including aerosol size distributions were also conducted from ice breaker cruises such as from the Swedish ice breaker Oden (Bigg and Leck, 2001; Covert et al., 1996; Heintzenberg and Leck, 2012; Leck and Bigg, 2005; Tjernström et al., 2014) and the Canadian Coast Guard Ship ice breaker Amundsen (e.g. Chang et al., 2011). Chang et al. (2011) used model calculations to show that the appearance of ultrafine particles can be explained by nucleation and growth attributed to the presence of high atmospheric and oceanic DMS concentrations measured at the same time. The Oden expeditions focus on the pack-ice-covered high Arctic, mainly north of 80N and also confirm the frequent presence of an UFP mode (e.g. Covert et al., 1996). The observations from the Oden cruises offer evidence that UFP in the inner Arctic might originate from primary sources (e.g. Heintzenberg et al., 2015; Karl et al., 2013). This is motivated by three main observations. First, a lack of sulfuric acid components in collected 15-50 nm particles (Leck and Bigg, 1999). Second, Leck and Bigg (2010) highlight that nucleation events in the high Arctic do not follow the classical banana shaped growth curve (Kulmala et al., 2001) but enhanced levels of ultrafine particles rather appear simultaneously in distinct size ranges (Karl et al., 2012). Third, such events could not be modelled with the selected empirical nucleation mechanism for the extremely low DMS concentrations in this region (Karl

et al., 2013). As a primary source marine microgels are suggested that might become airborne via the evaporation of fog and cloud droplets (Heintzenberg et al., 2006; Karl et al., 2013).

So far most studies that include size distribution measurements in the summertime Arctic were conducted from ground stations or ship cruises. To date there are only two studies that assess the altitude dependence of the size distribution:, i.e. one in the area of Svalbard (Engvall et al., 2008) and one from the Oden performing vertical profiles with a helicopter (Kupiszewski et al., 2013). Although no size distribution measurements were performed, Heintzenberg et al. (1991) measured vertical profiles of the total particle number concentration greater than 10 nm during June and July, 1984 over the Fram Strait-Spitsbergen area, and found a "rather uniform distribution" with altitude. Their measurements, however, were confined to 500 m-MSL and above.

In this study we present data from aerosol size distribution measurements taken from an aircraft during a three week period in July 2014 in the high Arctic area of Resolute Bay, Nunavut, Canada. The flights focused on vertical profiles from as low as 60 m above the ground up to 3km, as well as on low-level flights above different terrain such as fast ice, open ocean, polynyas and clouds. We focus especially on UFP (5-20 nm in diameter) and address the following questions: What are the concentrations of UFPs in the Arctic summertime, and what is their vertical distribution? What are the environmental conditions that favour occurrence of UFPs? And, is there evidence for growth of UFP to CCN sizes? Aside from the studies conducted near Svalbard, we believe this is the first aircraft study in the high Arctic to systematically address these specific questions. This work provides a comprehensive picture of UFPs observed during the campaign whereas a prior publication from Willis et al., (2016) detailed one UFP formation and growth event observed over Lancaster Sound.

2 Experimental

2.1 Sampling Platform Polar 6

The research aircraft Polar 6 owned by the Alfred Wegener Institute, Helmholtz Center for Polar and Marine Research, Bremerhaven, Germany served as the sampling platform. The Polar 6 is a

141 converted DC-3 airplane (Basler BT-67) modified to work under extreme cold weather
142 conditions. An advantage of the plane is that flights at very relatively low speeds and altitudes
143 (< 60 m a.g.l.) are possible. The cabin of the aircraft is non-pressurized. We maintained a
144 constant survey speed of approximately 120 knots (222 km h^{-1}) for measurement flights at
145 constant altitude, and ascent and descent rates of 150 m min^{-1} for vertical profiles. Instruments
146 and measurements specific to this paper are described below.

147 ### 2.1.1 Inlets

148 Aerosol was sampled through a stainless steel inlet mounted to the top of the plane and ahead of
149 the engines to exclude contamination. The tip of the inlet consisted of a shrouded diffuser that
150 provided nearly isokinetic flow. Inside the cabin the intake tubing was connected to a stainless
151 steel tube (outer diameter of 2.5 cm, inner diameter of 2.3 cm) that carried the aerosol to the back
152 of the aircraft where it was allowed to freely exhaust into the cabin so that the system was not
153 over-pressured. The stainless steel tube functioned as a manifold, off which angled inserts were
154 used to connect sample lines to the various instruments described below. In-flight air was pushed
155 through the line with a flow rate of approximately 55 L min^{-1} determined by the sum of the flows
156 drawn by the instruments (35 L min^{-1}), plus the flow measured at the exhaust of the sampling
157 manifold (20 L min^{-1}). A flow of 55 L min^{-1} was estimated to meet nearly isokinetic sampling
158 criteria at survey speed and the transmission of particles through the main inlet was
159 approximately unity for diameters between 20 nm to 1 μm (Leaitch et al., 2016). Although the
160 transfer of the aerosol from outside to the instruments is relatively fast (5 seconds or less),
161 volatilization of some components of the particles may have occurred. However, the growth of
162 newly formed particles by organic condensation occurs primarily by low volatility organic
163 components (e.g. Pierce et al., 2012). Thus, the integrity of the smaller particles is likely to have
164 been maintained. We do expect increasing line losses of particles with sizes decreasing from 10
165 nm. Therefore our observations will underestimate $N_{5\text{-}20}$.

166 Trace gases (CO and H_2O) were sampled through a separate inlet made of a 0.4 cm (outer
167 diameter) Teflon tube entering the aircraft at the main inlet and exiting through a rear-facing 0.95
168 cm exhaust line that provided a lower line pressure. The sample flow of approximately 12 L min^{-1}
169 was continuously monitored.

2.2 Instrumentation

2.2.1 Meteorological parameters and state parameters

Aircraft state parameters and meteorological measurements were performed with an AIMMS-20 manufactured by Aventech Research Inc. at a very high sampling frequency (>40Hz). The AIMMS-20 consists of three modules: (1) The Air Data Probe that measures the three-dimensional aircraft-relative flow vector (true air speed, angle-of-attack, and sideslip), and turbulence with a three-dimensional accelerometer. As well, temperature and humidity sensors are contained within this unit and provide an accuracy and resolution of 0.30 and 0.01 C for temperature and 2.0 and 0.1% for relative humidity measurements. (2) An Inertial Measurement Unit that consists of three gyros and three accelerometers providing the aircraft angular rate and acceleration; (4) A Global Positioning System for aircraft 3D position and inertial velocity. Horizontal and vertical wind speeds were measured with accuracies of 0.50 and 0.75 m s^{-1}, respectively. The high frequency raw data were processed to 1Hz resolution. Further details of the AIMMS including data processing can be found in (Aliabadi et al., 2016a).

2.2.2 Aerosol physical and chemical properties

Particle number concentrations and particle size distributions were measured with a TSI 3787 water-based ultrafine Condensation Particle Counter (UCPC), a Droplet Measurement Technology (DMT) Ultra High Sensitivity Aerosol Spectrometer (UHSAS) and a Brechtel Manufacturing Incorporated (BMI) Scanning Mobility System (SMS) coupled with a TSI 3010 Condensation Particle Counter (CPC). The UCPC detected particle concentrations of particles larger than 5nm in diameter with a time resolution of 1 Hz. The flow rate was set to 0.6 L min^{-1}. The particle concentrations measured by the UCPC are referred to as N_{tot} hereafter, noting as above that diffusional losses of particles smaller than 10 nm make the N_{tot} observations lower limits.

The BMI SMS was set to measure particle size distributions from 20nm to 100nm with a sample flow of 1 L min^{-1} and a sheath flow of 6 L min^{-1}. The duration of one scan was 40 s with a 20 s delay time before each scan resulting in a time resolution of 1min. The UHSAS performed size distribution measurements from 70 nm – 1 μm at a time resolution of 1 Hz with a sample flow

198 rate of 55 cm^3 min^{-1}. Details of the calibrations and instrument inter-comparisons performed
199 prior and during the campaign are described in detail in Leaitch et al. (2016).

200 Cloud condensation nuclei (CCN) were measured with a DMT CCN Counter (CCNC). The
201 CCNC was operated behind a constant pressure inlet that was set to 650 hPa. The nominal
202 supersaturation was held constant at 1%. Calibrations prior and during the campaign (for details
203 see Leaitch et al. 2016) showed that a nominal supersaturation of 1% at the reduced pressure
204 translated into 0.6% effective supersaturation.

205 Cloud droplet sizes from 2-45 μm were measured using a wing mounted Particle Measuring
206 System (PMS) FSSP 100. In this study these data are only used to identify periods when the
207 aircraft was flying in cloud. To avoid possible artefacts produced from shattering of cloud
208 droplets at the aerosol inlet, data from in-cloud times are discarded for the purposes of this study.

209 A DMT Single Particle Soot Photometer (SP2) was deployed to measure refractory black carbon
210 (rBC) number and mass concentrations. We refer to rBC mass concentrations as an indication of
211 pollution influence. Calibrations with Aquadag soot were performed prior to and during the
212 campaign. The lower size limit of detection of rBC particles by the SP2 was approximately
213 80nm.

214 Sub-micron aerosol composition was measured with an Aerodyne high-resolution time-of-flight
215 aerosol mass spectrometer (HR-ToF-AMS; e.g. DeCarlo et al., 2006). A detailed description of
216 the instrument is found in Willis et al. 2016. The main purpose of the instrument was to measure
217 non-refractory particulate matter such as sulfate, nitrate, ammonium, methane sulfonic acid
218 (MSA) and the sum of organics. Detection limits were 0.009, 0.008, 0.004, 0.005 and 0.08 μg m^{-3}
219 , respectively, for a 30 second averaging time.

220

221 ### 2.2.3 Trace gases

222 Carbon monoxide (CO) was measured with an Aerolaser ultra-fast carbon monoxide monitor
223 model AL 5002 based on VUV fluorimetry, employing the excitation of CO at 150 nm. In-situ
224 calibrations were performed during flight at regular intervals (15 – 30 min) using a NIST

traceable CO standard with zero water vapor concentration. CO mixing ratios were used as a relative indicator of aerosol influenced by pollution sources.

Water vapour (H_2O) measurements were based on infrared absorption using a LI-7200 enclosed CO_2/H_2O Analyzer from LI-COR Biosciences GmbH. The measurement uncertainty is ± 15 ppm_v. H_2O mixing ratios were used to calculate relative humidity with pressure and temperature measured by the AIMMS-20.

2.3 Data analysis and nomenclature of particle size data

All particle data were averaged to 1 min intervals to match the time resolution of the BMI SMS. Particle concentrations within different size intervals were calculated. The notation N_{a-b} is used; "a" gives the lower limit and "b" the upper limit of the calculated size interval. The BMI SMS was used to determine concentrations of particles from 20-90 nm diameter, and concentrations of particles larger than 90 nm diameter were determined by the UHSAS. If the size interval is expressed as $N_{>a}$ the upper limit is given by the detection limit of the UHSAS (1µm). Additionally, particle concentrations from 5-20 nm (short: N_{5-20}) were obtained by subtracting particle concentrations measured by the BMI SMS and by the UHSAS from the N_{tot} as determined by the CPC. The N_{5-20} are also referred to as ultrafine particles (UFP) in this study.

In order to obtain vertical profiles the data were averaged within altitude intervals. An average profile for a single flight was obtained by binning all data from the respective flight into altitude intervals of 100m starting at the lowest flight altitude. In addition to data obtained during vertical profile flights, data aquired while flying at a constant level were also included. Average profiles containing data from more than one flight were calculated by averaging the respective single flight profiles.

Average size distributions were obtained by simply averaging each bin for the desired time and altitude range. The size distributions measured by the BMI SMS were used for particle sizes from 20-90 nm, and the distributions at larger sizes are taken from the UHSAS. All particle concentrations are expressed for ambient pressure conditions, i.e. they have not been adjusted to standard temperature and pressure conditions. The N_{5-20} referred to as UFP are added to the size

distributions as additional bin assuming a bin width of 15 nm (from 5-20 nm) with the mid diameter of 12nm.

2.4 FLEXPART-WRF Simulations

We used FLEXPART-WRF (Brioude et al., 2013, website: flexpart.eu/wiki/FpLimitedareaWrf) simulations run backwards in time to analyse the origins of air masses sampled along the flight tracks. FLEXPART-WRF is a Lagrangian particle dispersion model based on FLEXPART (Stohl et al., 2005). Meteorological information is obtained from the Weather Research and Forecasting (WRF) Model (Skamarock et al., 2005). FLEXPART-WRF outputs retroplume information such as the residence time of air (over a unit area) prior to sampling. Residence times were integrated over the entire atmospheric column and 7 days backward in time. FLEXPART-WRF was run in two ways. First, one FLEXPART-WRF was completed for each flight using particle releases every 2 minutes along the flight track (100 m x 100 m x 100 m centered on the aircraft location) to produce potential emissions sensitivities (PES) that represent the average airmass origin for each flight. Second, separate runs were completed for points (every 10 minutes) along the flight track (100 m x 100 m x 100 m, 60 second release duration) in order to study different airmasses measured during the same flight. A more detailed description of the model as used for NETCARE 2014 is provided by Wentworth et al. (2015).

2.5 Study area and flight tracks

From July 4th to July 21st, 2014 eleven flights were conducted out of Resolute Bay (74.7 N, 95.0 W). In Figure 1 a compilation of all flight tracks on a satellite image is shown. The satellite picture was taken on July 4th, 2014 and reflects the situation of the region during period I (July 4 to July 12). Resolute Bay proved to be an ideal location for this study as we had access to both open ocean and ice covered regions. Additionally two polynyas were located north of Resolute Bay within the reach of our aircraft. Flights ranged between 4-6 hours. The flights covered two main areas: Lancaster Sound east of Resolute Bay and the area north of Resolute Bay where two

polynyas were located. The flights south of Resolute Bay in Lancaster Sound concentrated around the ice edge.

The ice/water coverage visible on the satellite picture is representative for the area during the first period. As can be seen, the ice edge was situated about 150 km east of Resolute Bay. It is clearly visible in the satellite image as a sharp line. The transition from a completely ice covered region to open ocean was very abrupt during the first period. Only after a period of bad weather with high winds did the ice edge become less clear, and the region starting about 80 km east of Resolute Bay to about 200 km east was covered by fractured ice.

Roughly 50% of the flight time was within the inversion layer, and 50% was in the free troposphere conducting altitude profile flights. A considerable amount of time was spent at 2800 m as this was the preferred altitude when travelling to a certain area. When clouds were present, the aircraft sampled them by slant profiling through the cloud in the case clouds were above the boundary layer, or, in the case clouds were within 200 m of the surface, by descending into the cloud as low as possible. Aerosol observations while inside cloud are excluded from the analysis here due to potential artifacts from droplets shattering on the outside inlet.

3 Meteorological and atmospheric conditions

Meteorological conditions changed over the course of the campaign. Similar conditions were encountered during the first part of the campaign (July 4th – July 12th, 6 flights), referred to as the "Arctic air mass period" because air masses from within the Arctic dominated and the atmosphere showed structures typical for the Arctic such as a low boundary layer height with thermally stable conditions, indicated by a near surface temperature inversion, and frequent formation of low level clouds. At this time Resolute Bay was under the influence of high pressure systems. Clear sky with few or scattered clouds and low wind speeds dominated. Conditions changed starting from July 13th when the region was influenced by troughs of a low pressure system located to the west above Beaufort Sea, which eventually passed through Resolute Bay on July 15th bringing along humidity, precipitation and fog. Intense fog and low visibility impeded flying from July 13th to July 16th. A short good weather window in which the

307 fog dissipated permitted flying again on July 17th (referred to as “transition day”; one flight) just
308 before Resolute Bay came under influence of a pronounced low pressure system located to the
309 south with its center around King William Island (69.0 N, 97.6 W). The last campaign days
310 (referred to as “southern air mass period”, three flights) were characterised by the influence of
311 this pronounced low pressure system bringing air masses from the south and providing higher
312 wind speeds, an overcast sky and occasional precipitation.
313
314 Vertical profiles of median temperature, relative humidity (RH), wind speed, CO and N_{tot} (Figure
315 2) illustrate median atmospheric conditions during the measurement flights. Prominent features
316 representing the trend of each period and reflecting the general meteorological situation will be
317 described here, with details discussed in the respective sections. The Arctic air mass period was
318 characterized by frequent thermally stable conditions within the near surface layer , representing
319 typical conditions during the Arctic summertime (Aliabadi et al., 2016a; Tjernström et al., 2012).
320 The median temperature profiles show that on average the boundary layer reached up to ~300 m
321 with a temperature increase of about 5 C. In this paper we will refer to this part of the
322 atmosphere as the boundary layer (BL) and to the air masses above as the free troposphere (FT).
323 A BL height of 300m corresponds well to the boundary layer height of 275 +/- 164 m estimated
324 by (Aliabadi et al., 2016a) using the method of bulk Richardson number (Aliabadi et al., 2016b)
325 and a critical bulk Richardson number of 0.5, using data from radiosondes launched at Resolute
326 Bay and the Amundsen icebreaker, which also performed research operations in Lancaster sound
327 during the campaign period.

328 Within the BL particle concentrations spanned over a wide range of concentrations (max N_{tot}:
329 ~10000; median values: ~150 to ~1700 cm^{-3}). Highest N_{tot} occurred during the Arctic air mass
330 period, while N_{tot} was constantly low within the lower atmosphere on the transition day. Median
331 temperatures near the surface ranged from -1 C to 5 C during the Arctic air mass period, largely
332 depending on the terrain below (e.g. ice or open water) and were clearly higher during when the
333 southern air masses arrived (e.g. at the “surface”: 4 C and 7 C, respectively) and, if present, the
334 BL was less pronounced. The higher temperatures coincide with the influence of low pressure
335 systems bringing warmer air masses from the west and south and additional higher wind speeds
336 providing a better mixing of the atmospheric layers (5.6 ms^{-1} vs 12m^{-1} near the surface). CO

mixing ratios were extremely low during the Arctic air mass period (median: 78.3 ppb_v) and on the transition day (median: 83.4 ppb_v) indicating pristine air masses that had not recently been affected by pollution or biomass burning sources. During the southern air mass influence CO mixing ratios clearly increased (median: 95.0 ppb_v) confirming a change in air mass and suggesting possible influences by pollution sources and wild fires in the North West Territories (Supplementary Figure 2). Relative humidity profiles show that the near surface layer of the atmosphere was very moist with RH > 80 % during all periods.

4 Results and Discussion

4.1 Ultrafine particle events

4.1.1 Frequency of ultrafine particle events

Throughout the campaign we observed large variability in particle concentrations (Figure 3). We observed not only very clean air masses with N_{tot} of a few tens cm^{-3} (with the lowest 1-second value of 1 cm^{-3}), but also concentrations as high as a few thousands per cm^{-3} (with the highest value of 10000 cm^{-3}). The highest and lowest concentrations were measured within the BL (Figure 3b). Above the BL (Figure 3b) particle concentrations were relatively constant where 60% of the time concentrations were between 200 - 300 cm^{-3} (for a discussion of the average size distribution see sections 4.1.2 - 4.1.4). Especially during the Arctic air mass period (Figure 2) the atmosphere was characterized by a strong contrast between the BL and the FT.

UFP were very frequently present within the BL in high concentrations (Figure 3c). Here we refer to "bursts" of particles as a sudden and relatively large increase in N_{5-20}: concentrations suddenly rising from tens cm^{-3} to several hundreds and thousands cm^{-3}. This may reflect inhomogeneities in the NPF process or reflect the aircraft flying in and out of areas of high UFP concentrations. Bursts of N_{5-20} > 2000/cm^3 were observed over polynyas, consistent with previous observations (Leaitch et al., 1984; 1994), in Lancaster Sound and south of Resolute Bay. The N_{5-20} was higher than 200 cm^{-3} during 65% of the time. Indeed, high N_{tot} was mainly driven by UFP (as can be seen by comparison of black dots indicating high N_{tot} in Figure 3c and

high UFP in Figure 3d). Whenever N_{tot} is greater than 2000 cm^{-3}, UFP was larger than 1000 cm^{-3}. This is also illustrated by the ratio of UFP/N_{tot} (Figure 3e). A ratio of zero means that no UFP were present, while a ratio of one means that only UFP were present. Within the boundary layer 32% of the time the size distribution was dominated by UFP (ratio > 0.5).

The frequent presence of UFP agrees well with other studies made during the Arctic summertime at several locations, such as at the ground stations in Ny Alesund and Zeppelin (Ström et al., 2009; Tunved et al., 2013), at Alert (Leaitch et al., 2013), and from ship-based observations (Chang et al., 2011; Covert et al., 1996; Heintzenberg et al., 2006). However, such a frequent presence of an UFP mode (65% of the time > 200 cm^{-3}) in the BL is unique to this study. Possible reasons for the higher occurrence of UFP might be the combination of the proximity of open ocean (providing a source of UFP or precursor gases), favourable meteorological conditions (sunny weather, inversion layer with cloud formation) and very clean air masses with low condensation sinks. Also, since observations of UFP were one focus of this study, the fractional occurrence of the UFP mode may be biased slightly high due to longer sampling times associated with UFP occurrence. Calm weather conditions may have been another factor. The highest concentrations of UFP were measured at lower wind speeds (< 5m s^{-1}; Supplementary Figure 1), while lower UFP concentrations (1000 cm^{-3}) were found at higher wind speeds (>12ms^{-1}) suggesting a dilution effect of the wind. Such a dilution effect implies proximity to the source.

In the following sections, the vertical distribution of UFP and the size distributions are discussed in relation to meteorological conditions during the three distinct periods that characterized this campaign.

4.1.2 Arctic air mass period: July 4th to July 12th

During this first period the study area was under the influence of a high pressure system. As illustrated by FLEXPART-WRF results (Figure 4a and 4b), air masses were either coming from the North extending to the east in the Arctic Ocean or from the East passing over the open ocean in Lancaster Sound and Baffin Bay. Both examples indicate that air masses resided within the

392 Arctic region at least 5 days prior to sampling. This is true for all flights during this period. The
393 very low CO mixing ratios (78 ppb_v, see Figure 2) and average BC mass concentrations of 3 ng
394 m^{-3} (not shown) confirm that air masses were very clean and without recent influence from
395 pollution sources. As discussed in section 3, temperature profiles indicate thermally stable
396 conditions in the lowest layers with near-surface temperature inversions. During almost all
397 vertical profiles we observed temperature inversions of about 4-6 C near the surface. Such an
398 atmospheric structure i.e. a shallow boundary layer is typical for the Arctic summertime (e.g.
399 Aliabadi et al., 2016a; Tjernström et al., 2012).

400 The Arctic air mass period was characterized by a very sharp contrast between the BL and the
401 FT in terms of particle number concentrations and sizes (Figure 5). The BL was characterized by
402 a prominent layer of UFP from the surface to about 300 m with the highest concentrations closest
403 to the surface (Figure 5a). The height of the UFP layer coincides with the average height of the
404 temperature inversion for this period (see temperature profile Figure 2) and indicates that air
405 masses were stably layered limiting exchange with the FT. This is supported by the observed
406 lower turbulent mixing (i.e. turbulent kinetic energy) from boundary layer to the free troposphere
407 during the campaign (Aliabadi et al., 2016a).

408 During this period we measured the highest concentrations of UFPs with the one minute average
409 up to 5300 cm^{-3}. On a typical flight several bursts (see Section 4.1.1) of high UFP concentrations
410 were encountered in the BL. Particle bursts lasted from a few seconds to several minutes,
411 corresponding to a spatial extent of several hundreds of meters to dozens of kilometers. The large
412 spatial variability is also illustrated by the frequency distribution of UFP in the BL shown in
413 Figure 5c: 40% of the time concentrations of UFP were larger than 200 cm^{-3}, 11% of the time
414 larger than 1000 cm^{-3} and 3% of the time even larger than 2000 cm^{-3}. Particle concentrations in
415 the FT are relatively uniform, and concentrations of UFP were less than 50 cm^{-3} up to 1200m and
416 ~10 cm^{-3} above.

417 The average $N_{20\text{-}40}$ is similar to the UFP, showing a maximum in its concentration at the same
418 altitude. The concentrations of larger particles ($N_{>40}$, $N_{>80}$, $N_{>150}$) are much lower in the clean BL
419 (surface areas of ~5μm^2 m^{-3} and lower). However, the $N_{>40}$ and $N_{>80}$ increase from the lowest
420 altitude to the next averaged altitude, consistent with the increase in the UFP and $N_{20\text{-}40}$. These

results suggest that some of the UFP experienced growth to sizes of 20-80 nm within a few hours, as demonstrated by Willis et al. (2016). Within the FT particle concentrations were surprisingly uniform and concentrations of UFP were less than 50 cm^{-3} up to 1200m and ~10 cm^{-3} above.

In Figure 5b, the median size distribution shows that increases in UPF in the BL were frequent. The average size distribution shows that at times higher concentrations of particles extended up to about 80 nm, consistent with the suggestion above that some UFP particles experienced growth to larger sizes. A relevant case will be discussed in Section 4.3. Occasionally a mode of particles larger than 400 nm was present in the BL over open water (see Section 4.2), which was likely the product of primary oceanic emissions.

4.1.3 Transition day on July 17th

July 17th marks the transition from dominance by Arctic air masses to a more distant influence from southern air masses. The transition day consists of only one flight in the area of Lancaster Sound, during which low concentrations of particles larger than 20 nm were observed below 600 m: e.g. $N_{>40}$ ranged from 60 cm^{-3} to 100 cm^{-3}; see Figure 6. The deeper layer of lower concentrations may have been a result of cloud processing and scavenging. During the days before flying was impossible because of intense fog and cloud at Resolute Bay. A different transport regime may also have contributed to this situation. On this day the low pressure system situated to the west was bringing air masses from the west along the Canadian and Alaskan coastline (Figure 4c). The temperature profile shows an inversion between 650-1000m possibly indicating a change in air mass. CO mixing ratios (83ppb_v) and BC mass concentrations (3ng/cm^{-3}) were also quite low indicating mostly Arctic background conditions.

On this day, occasional bursts of UFP up to 1400-1900 cm^{-3} were observed within the bounday layer (Figure 6b). UFP of 200 cm^{-3} or more were observed about 20% of the time (Figure 6c), and the average concentration was 240 cm^{-3} at the lowest level of the profile (Fig. 6a). Concentrations of larger particles ($N_{>40}$, $N_{>80}$, $N_{>150}$) increased sharply at about 700m coinciding with the temperature inversion. The very low concentrations of larger particles ($N_{>150}$: <10 cm^{-3})

below the temperature inversion are very similar to the conditions encountered within the BL during the previous period. As above, the differences in the transition day below 700 m may have been due to a combination of fog/cloud scavenging and a change of air mass. Median and average size distributions indicate a minimum at around 65nm that might be the result of cloud processing (Hoppel et al., 1994), consistent with the Arctic observations of (Heintzenberg et al., 2006) and the activation diameters observed during this study (Leaitch et al., 2016).

4.1.4 Southern air mass period: July 19th – July 21st

During this period the region was under the influence of a low pressure system centered south of Resolute Bay. FLEXPART-WRF air mass trajectories (Figures 4d and 4e) indicate a prevalence of air masses from the south potentially affected by wild fires (see Supplementary Figure 2). At the beginning of this period on July 19th (Figure 4d), air mass trajectories suggest the strongest influence from the south while towards the end of the period on July 21st (Figure 4e), FLEXPART-WRF indicates that southern air masses mixed with air masses coming off Greenland. Near surface temperatures were higher than during the previous periods (Figure 2) and temperature inversions were less pronounced (2-4 C) and not observed at all locations suggesting a less stable lower atmosphere. On July 19th we encountered the highest wind speeds in the BL (16 m/s within the near surface layer and 20 m/s slightly above). Also RH was relatively high near the surface (91%) and did not drop below 80% throughout the vertical atmosphere. CO mixing ratios were higher than during the prior periods suggesting that the air was at times influenced by pollution or biomass burning.

UFP were observed less frequently than during the Arctic air mass period and in lower concentrations (Figure 7). Bursts of UFP above 1000 cm^{-3} occurred only at three locations, all during the flight on July 21st. Average UFP concentrations were only approximately 190 cm^{-3}. UFP concentrations of 200 cm^{-3} or higher were detected 31% of the time below 300m (Figure 7c).

The southern air mass period clearly shows different aerosol characteristics within the near surface layer than compared to the Arctic air mass period and the transition day. Average concentrations of particles larger than 40 nm were highest within the boundary layer and

decreased with altitude (Figure 7a). This is in sharp contrast to the cleaner boundary layers observed before. Whereas concentrations of particles larger 40nm were ~100 cm^{-3} and lower during both prior periods, they were as high as 300 cm^{-3} for this period. Even large accumulation mode particles ($N_{>150}$) averaged ~50 cm^{-3} (compared to 10 cm^{-3} for both previous periods). Also, both the median and average size distributions show a pronounced mode of particles larger than 500 nm within the BL (Figure 7b). Primary emissions from the sea spray promoted by the higher surface wind speeds (see Figure 2) are likely a factor contributing to the larger particles.

During the southern air mass period, three important factors had changed compared to both prior periods. (1) Air mass back trajectories had clearly shifted to the south and potentially transported emissions from wild fires located in the Northwest Territories (Supplementary Figure 2) into the region, which might mix into the boundary layer. (2) The Amundsen ice breaker was present in Lancaster Sound and acted as a local pollution source. (3) Wind speeds were higher and the ocean was visibly turbulent with breaking waves that might enhance primary oceanic aerosol emissions. The increased condensation sinks from these potential sources in combination with other factors (e.g. reduced sun light) and relatively low residence times of air masses within the boundary layer (compared to the Arctic air mass period) may explain the relatively low and infrequent concentrations of UFPs.

Within the FT the size distributions shows a bimodal character with a minima at 60-80 nm, which may indicate the air masses experienced cloud processing. This is likely, given the presence of the low pressure system bringing moister and warmer air masses. The bimodal size distribution is different from the average size distribution during the Arctic air mass period when drier air masses from within the Arctic dominated.

4.2 UFP occurrence above ice versus water

We investigated the potential influence of different underlying water surfaces on the occurrence of UFP by examining in detail the time periods when we were flying at altitudes at or below 500 m during the Arctic air mass period. We distinguish between three water surfaces: ice covered areas (including ice edge and ice covered with melt ponds), open ocean (including polynyas), and low-level clouds (including both cloud above water and cloud above ice). Here we point out

505 that the case "cloud" does not include in-cloud flight times but only flight periods when above
506 cloud top without actually entering the cloud (confirmed by a zero signal in a liquid cloud probe
507 (FSSP100)). An altitude of 500 m was chosen to include time periods when we were flying
508 above low-level clouds and to capture mostly flights within the boundary layer where a local
509 influence of the terrain below was likely. During the Arctic air mass period, there was a clear
510 separation between ice and open water over Lancaster Sound with east of the ice edge
511 completely ice free, while west of the ice edge the ocean was seamlessly covered by fast ice (see
512 satellite picture in Figure 1).

513 Each average profile above the different water surface exhibits unique features (Figure 8). Above
514 ice the highest concentrations of UFP (average: 400 cm^{-3}) were found nearer the surface (70 m)
515 and the N_{tot} are slightly higher (580). In the BL over open water, the N_{tot} and UFP number
516 concentrations are 900 cm^{-3} and 560 cm^{-3}, respectively, and in the air just above cloud, the
517 average N_{tot} and UFP number concentrations are 2000 cm^{-3} and 1040 cm^{-3}, respectively. In the
518 open water and cloud cases, the highest concentrations of ultrafines are at the point of
519 measurement closest to the water surface. In the cloud case and open water case, the N_{20-40}
520 particles show an increase at the same time as the N_{tot} and UFP suggesting that the UFP form and
521 grow to larger sizes. This is not observed in the over-ice case, which suggests that some of the
522 new particles could have formed elsewhere (e.g. over open water) and been transported over the
523 ice, or that the growth rates over ice are slow. In all three cases, the largest particles show
524 relatively smaller abundances at the lowest altitudes samples. An increased abundance of UFP at
525 lower surface areas supports the hypothesis that UFP form via nucleation of precursor gases.

526 ### 4.3 Case study: July 8

527 The flight on July 8 provides a case study illustrating that the occurrence of UFP is confined to
528 the BL suggesting a surface source of UFP and that the appearance of UFP is promoted by cloud.
529 We consider the altitude dependence of the UFP within the BL in relation to air mass history and
530 cloud.

531 On this flight we first flew out into Lancaster Sound west of Resolute Bay, turned around and
532 descended into the BL above the ice. Here, we focus on the time period from 15:50 UTC

(descent into the BL) to 17:20 UTC where we travelled from west to east and remained within the BL but stayed out of cloud as shown in Figure 9; see also Supplementary Figure 2. The later part of the flight focused on in-situ cloud properties and is discussed elsewhere (Leaitch et al., 2016). The weather was sunny with low level clouds starting around 150 km over ice and west of the ice edge in Lancaster Sound. The clouds had formed over the water and were blown over the ice where they were dissipating (Leaitch et al., 2016). In the entire area the atmosphere was characterized by a surface temperature inversion extending vertically up to about 300 m with ~1 C near the surface and ~5 C at 300 m and was accompanied by decreasing relative humidity (Figure 9f). Local low-level winds were predominantly from the south to east and wind speeds were below 5 ms^{-1}.

UFP were present throughout the BL with the highest concentrations at the lowest altitudes and decreasing concentrations towards the top of the BL (Figure 9b). In contrast, larger particles (e.g. $N_{>40}$) exhibit the opposite pattern, with lower concentrations at lower altitudes and higher concentrations at higher altitudes. Six locations from west to east (points A-F in Figure 9a) are used to illustrate the changing aerosol characteristics. Location A is situated well above the BL and at this point no UFP were present (detailed size distributions are shown in Supplementary Figure 4). At location B, the point at which we first entered the BL, an UFP mode (~370 cm^{-3}) was present at 60m, while UFP concentrations were lower at slightly higher altitudes (~80 cm^{-3} at 230 m) such as location C. At the lower altitudes the UFP concentrations gradually increased as we approached the ice edge. The most striking observation is the steep increase in particle concentrations at about 60 km west of the ice edge (location D) where UFP increased to above 4000 cm^{-3} at 150 m or just above cloud top. At the same time N_{20-40} concentrations showed a similar increase. The increased UFP concentrations were vertically limited to near cloud top and decreased rapidly with increasing altitude. The same pattern is also observed for temperature, H_2O and CO_2 (Figure 9g) suggesting the existence of a distinct air mass at the surface that gets diluted into the air mass above. Further east the flight was restricted to a slightly higher altitude above cloud top. At point F, where we were close to the BL top, no peaks in particle concentrations were observed. At point E, just before the ice edge, between the top of cloud and the top of the BL, UFP concentations reached about 3400 cm^{-3}.

562 Air mass histories at these locations determined from FLEXPART-WRF (Figure 10) indicate the
563 following:
564 (1) To the west of Resolute Bay (point B) Lancaster Sound air masses had been mixed with air
565 masses from the North. This is also confirmed by the local wind directions indicating winds
566 coming from the Northwest sector (Figure 10a), and it is consistent with the associated change in
567 cloud. (2) Near the top of the BL, air masses had descended recently (< 3 h) into the BL (Figure
568 10c point C and point F). (3) In contrast, deeper within the BL at points B and D air masses had
569 descended into the BL earlier (~20 h) before arriving at the point of observation. In the case of
570 point D, where we observed the largest mode of UFP extending above 40nm, air masses had
571 been travelling from the east exclusively over the open waters in Lancaster Sound during the last
572 day before arriving at the point of observation.

573 Aerosol composition shows a clear difference between the aerosol in the FT and the BL. The
574 aerosol sulphate rapidly decreases as we enter the BL around 16:00, while aerosol organic mass
575 concentrations show an initial relative increase followed by an absolute increase towards the east
576 (Figure 9c). Within the BL aerosol organics and sulphate mass loadings show a pattern similar to
577 $N_{>40}$ and $N_{>80}$. Both decrease each time we descended deeper into the BL. However, at the same
578 time the organics-to-sulphate ratio indicates that the relative contribution of organics to aerosol
579 mass increases at lower altitudes and especially above cloud (Figure 9e). Well within the
580 inversion layer and in the vicinity of cloud top the aerosol was dominated by organics. At the
581 same time also ratio of MSA to sulphate was higher (Figure 9e), suggesting a marine biogenic
582 influence of the aerosol sulphur. The marine biogenic influence at the lower altitudes agrees well
583 with the FLEXPART-WRF simulations showing that air masses at this altitude had spent almost
584 an entire day exposed to the open waters in Lancaster Sound. Consistent with the higher organic
585 content measured with the AMS, the single particle aerosol mass spectrometer ALABAMA
586 (Brands et al., 2011; Willis et al., 2016) detected a higher fraction of trimethylamine (TMA)-
587 containing particles for particles larger than 150 nm in diameter (F. Köllner, personal
588 communication, July 2016). Gaseous TMA emissions from marine biogenic origin (Ge et al.,
589 2011; Gibb et al., 1999) may have additionally favored the subsequent growth of the freshly
590 nucleated particles by condensation. Another possibility may be uptake of TMA in the cloud
591 phase (Rehbein et al., 2011) if the particles have grown to sufficiently large sizes to be activated

as CCN. Interestingly, compared to other days these TMA-containing particles are smaller and to a lesser degree internally mixed with potassium and levoglucosan which supports the hypothesis of ultrafine particles originating from nucleation in a biogenic marine environment and subsequent growth.

To explain these observations, we hypothesize that the smaller particle mode is formed by nucleation and growth occurring within the BL and especially in cloud vicinity. UFP concentrations near cloud top have been reported before (e.g. Radke and Hobbs 1991, Wiedensohler et al. 1997, Clarke et al., 1999; Garrett et al., 2002; Hegg et al., 1990; Mauldin et al., 1997) and it is suggested that nucleation in near cloud regions is favoured by the low surface areas, possibly due to cloud scavenged aerosol, moist air and a high actinic flux. Indeed, near cloud top where we observed an increase of UFP extending up to almost 50 nm the conditions for nucleation and growth are ideal. We speculate that the availability of precursor gases is provided by the long residence time (~20h) of the air masses over open water (Figure 10, point D). In other words, precipitating clouds scavenge aerosol particles, reducing the surface area for condensation, but some fraction of nucleation precursor gases with lower Henry's Law constants can pass through (e.g. SO_2) leaving the potential for H_2SO_4 in the higher OH in the cloud outflow (a discussion of the processes can be found in Seinfeld and Pandis, 1998). The very high organic loadings and MSA to sulphate ratio likely indicate that the formation and growth of these particles is driven by a combination of DMS and organic precursors (volatile organic compounds) that are emitted by the open ocean in Lancaster Sound (e.g. Chang et al., 2011; Sjostedt et al., 2012; Mungall et al., 2016).

The event at point E occurs where the aircraft was between cloud top and the top of the BL, where no increases in UFP were observed before or after. It may be that the aircraft descended slightly but sufficiently into the cloud-influenced area, which looks to be 25-40 m above cloud top (Figure 9g), but also at that point we were in vicinity of Prince Leopold Island which is a bird sanctuary and many bird colonies nest at the 260m high cliff. FLEXPART-WRF and the in-situ wind measurement show that air masses to a large extent were directly coming off the island (Figure 10, point E) suggesting a connection between the appearance of UFP and possible emissions from the fauna of the island. The increase of particle phase ammonium (Figure 9d) at

621 the same time supports this connection and nucleation of particles from biogenic precursors
622 emitted by bird colonies are documented (Weber et al., 1998; Wentworth et al., 2016, Croft et al.
623 2016b).

624 Alternatively, it should be considered that evaporating fog and cloud droplets may also act as a
625 primary source of UFP (e.g. Heintzenberg et al., 2006; Karl et al., 2013; Leck and Bigg, 1999).
626 Karl et al., (2013) suggested a combined pathway that involves the emission of UFP by fog and
627 cloud droplets, together with secondary processes enabling growth of these particles. For our
628 observations we have no reason to assume that nucleation does not occur since conditions are
629 ideal but we cannot rule out that nanoparticles are emitted by the possibly evaporating cloud
630 droplets onto which gases then condense.

631 In conclusion the aerosol mass within the near surface layer is dominated by organics relative to
632 sulphate, while at just slightly higher altitude sulphate is clearly increased and increases further
633 above the inversion layer. A high organic content coincides with increases in UFP particles,
634 especially at times when also growth into the size range up to 50nm is indicated. Similarly the
635 MSA-to-sulphate ratio shows a peak at the lowest altitudes with maximum values in the vicinity
636 of clouds that coincide with a long residence time (~20h) of the air masses within the BL and
637 above open water. The data thereby suggest a marine biogenic influence of the aerosol within the
638 lower layers of the atmosphere. We note that similarly high levels of aerosol organics and MSA
639 were observed during the flight on July 12 associated with a NPF event and growth but in cloud-
640 free conditions Willis et al. (2016).

641 ### 4.4 CCN activity

642 CCN concentrations were measured at a supersaturation of 0.6%. The vertical profiles of CCN
643 concentrations (Figure 11a) show patterns similar to those of larger particles. In the very clean
644 boundary layer of the Arctic air mass period and the transition day CCN concentrations are
645 equally low (~70 cm^{-3} and ~50 cm^{-3}, respectively). In contrast, southern air mass period average
646 BL CCN concentrations are amongst the highest observed during this campaign (>300 cm^{-3}).
647 Within the free troposphere CCN concentrations are surprisingly constant during the Arctic air
648 mass period (120 ± 27 cm^{-3}) and more variable on the transition day (92 ± 46 cm^{-3}) and the

649 southern air mass period (103 ± 67 cm^{-3}). The constant CCN concentrations during the Arctic air
650 mass period correspond to the very uniform atmosphere dominated by aged aerosols we
651 observed during this period and to the more layered atmosphere influenced by southern air
652 masses possibly contaminated by biomass burning plumes during the later period. Correlations
653 with $N_{>80}$ (Figure 11b) confirm that larger particles are a good approximation for these CCN
654 concentrations. On average CCN concentrations agree to within ± 20 % of $N_{>80}$. However, it
655 should be noted that slight differences between the 3 periods are indicated in the correlation
656 curves: during the Arctic air mass period the average activation diameters are smaller than 80
657 nm, and during the southern air mass period they are larger than 80 nm. Assuming uniform
658 chemical composition throughout the particle size range, an activation diameter of 80 nm at 0.6%
659 supersaturation indicates an aerosol much less hygroscopic than, for example, ammonium
660 sulphate; pure ammonium sulphate particles would activate at 40 m at 0.6% supersaturation. For
661 the one specific event during which growth occurred (Willis et al., 2016), it was demonstrated
662 that high CCN concentrations coincide with elevated organic mass loading. The reduced
663 hygroscopicity of organic material relative to soluble inorganic salts (Petters and Kreidenweis,
664 2007) can explain the larger effective activation diameter.

665 A central question is whether and to what degree the CCN are influenced by the UFP. Two
666 factors help with addressing this question: 1) particles as small as 20 nm and in general much
667 smaller than the average 80 nm size associated with the CCN at 0.6% will nucleate cloud
668 droplets in the clean environment of the summer Arctic (Leaitch et al., 2016); 2) there is
669 evidence here that increases in particles larger than 20 nm are associated with increases in the
670 UFP, particularly for UFP influenced by cloud (e.g. Figure 8). Figure 12 shows regressions of
671 CCN with UFP, $N_{>20}$, $N_{>30}$, $N_{>40}$ and $N_{>50}$. The high variability in the UFP and the time needed
672 for a UFP particle to grow to an average size of 80 nm under these low precursor levels does not
673 permit a direct connection of the CCN and UFP, but in all other cases, the main clusters of the
674 regressions show quite similar and strong connections with the CCN measurements.
675 Associations of the UFP with the $N_{>20}$ in the BL mean that some of these UFP are able to
676 contribute to cloud-nucleating particles.

677

5 Discussion and Conclusions

This study presents airborne observations of ultrafine particles (UFP) during the Arctic summertime. Eleven flights were conducted in July 2014 in the area of Resolute Bay situated in the Canadian Archipelago. The location allowed access to open water, ice-covered regions and low clouds. Flights focused around the ice edge in Lancaster Sound including open waters to the east, the ice-covered region to the west, and polynas north of Resolute Bay. UFP were observed within all regions and above all terrains with the highest concentrations encountered in the boundary layer immediately above cloud and open water. It is shown that UFP occur most frequently (>65 % of the time) and with the highest concentrations (up to 5300 cm^{-3}) during an Arctic air mass period when the air is very clean and the boundary layer is thermally stable.

The frequent presence of UFP in the boundary layer over open water and low cloud and the enhanced number concentrations at the lowest altitudes sampled indicate a surface source, such as the ocean, for the UFP gaseous precursors. This is especially true during the Arctic air mass period when the sampling region was pristine and not influenced by pollution. FLEXPART-WRF simulations indicate that air masses had resided within the Arctic region at least 5-7 days prior to sampling. During this time UFP were restricted to the boundary layer and no UFP events were observed aloft, thereby excluding that these UFP form in the free troposphere and subside into the near surface layer e.g. (Clarke et al., 1998; Quinn and Bates, 2011). At the same time we observed an extremely clean boundary layer (surface area of $N_{>40}$ ~5 $\mu m^2 m^{-3}$). Low surface areas increase the probability of particle formation via nucleation by reducing the surfaces for precursor gases to condense on.

Chlorophyll-a concentrations (Supplementary Figure 5) indicate a relatively high level of biological activity of the ocean (such as phytoplankton blooms known to produce DMS) throughout Lancaster Sound, to the east in Baffin Bay and in the open waters of the polynyas during the time period of the study. Indeed, measurements in Lancaster Sound performed from the Amundsen ice breaker just a few days after the aircraft campaign show that gas-phase DMS mixing ratios were high in the Lancaster Sound region (Mungall et al., 2016), up to 1155 ppt_v. DMS was also measured from the Polar 6 aircraft with an offline technique. Maximum mixing ratios of 110 ppt_v were detected in the surface layer (R. Ghahremaninezhad; personal

communication), again confirming a marine influence in the boundary layer. The measured DMS concentrations are above the nucleation threshold obtained by modelling performed in the study of Chang et al. (2011) who concluded that DMS mixing ratios of $\geq$ 100ppt$_v$ are sufficient to account for the formation of hundreds of UFP when background particle concentrations are low.

Relating observations of UFP to the surface below during the Arctic air mass period revealed that the highest UFP concentrations occurred above low-level cloud and open water with averages of 1040 cm^{-3} and 560 cm^{-3}, respectively. Above low-level cloud N_{20-40} showed increased concentrations. This simultaneous increase in concentrations suggests that UFP grow into the 40 nm size range, where they can nucleate cloud droplets.

Overall, the summertime Arctic is an active region in terms of new particle formation, occasionally accompanied by growth. The value of these altitude profiles across a wide spatial extent, performed for the first time in this campaign, is that they demonstrate that this activity is largely confined to the boundary layer, and that the dominant source of small particles to the boundary layer does not arise by mixing from aloft but most likely from marine sources. For future studies, the relative impact of such natural sources of UFP needs to be evaluated with respect to potential new sources, such as may arise with increasing shipping.

Acknowledgements

The authors would like to thank a large number of people for their contributions to this work. We thank Kenn Borek Air, in particular the pilots Kevin Elke and John Bayes and the aircraft engineer Kevin Riehl. We are grateful to John Ford, David Heath and the University of Toronto machine shop for safely mounting our instruments on racks for aircraft deployment. We thank Jim Hodgson and Lake Central Air Services in Muskoka, Jim Watson (Scale Modelbuilders, Inc.), Julia Binder and Martin Gerhmann (Alfred Wegener Institute, Helmholtz Center for Polar Marine Research, AWI), Mike Harwood and Andrew Elford (Environment and Climate Change Canada, ECCC), for their support of the integration of the instrumentation and aircraft. We gratefully acknowledge Carrie Taylor (ECCC), Bob Christensen (U of T), Lukas Kandora, Manuel Sellmann and Jens Herrmann (AWI), Desiree Toom, Sangeeta Sharma, Dan Veber, Andrew Platt, Anne Marie Macdonald, Ralf Staebler and Maurice Watt (ECCC) for their support

of the study. We thank the Biogeochemistry department of MPIC for providing the CO instrument and Dieter Scharffe for his support during the preparation phase of the campaign. The authors J.L. Thomas and K.S. Law acknowledge funding support from the European Union under Grant Agreement n_ 5265863 – ACCESS (Arctic Climate Change, Economy and Society) project (2012-2015) and TOTAL SA. Computer simulations were performed on the IPSL mesoscale computer center (Mésocentre IPSL), which includes support for calculations and data storage facilities. We thank the Nunavut Research Institute and the Nunavut Impact Review Board for licensing the study. Logistical support in Resolute Bay was provided by the Polar Continental Shelf Project (PCSP) of Natural Resources Canada under PCSP Field Project #218614, and we are particularly grateful to Tim McCagherty and Jodi MacGregor of the PCSP. Funding for this work was provided by the Natural Sciences and Engineering Research Council of Canada through the NETCARE project of the Climate Change and Atmospheric Research Program, the Alfred Wegener Institute, Helmholtz Center for Polar and Marine Research and Environment and Climate Change Canada.

References

Aliabadi, A. A., Staebler, R. M., Liu, M. and Herber, A.: Characterization and Parametrization of Reynolds Stress and Turbulent Heat Flux in the Stably-Stratified Lower Arctic Troposphere Using Aircraft Measurements, Boundary-Layer Meteorol., doi:10.1007/s10546-016-0164-7, 2016a.

Aliabadi, A. A., Staebler, R. M., de Grandpré, J., Zadra, A. and Vaillancourt, P. A.: Comparison of Estimated Atmospheric Boundary Layer Mixing Height in the Arctic and Southern Great Plains under Statically Stable Conditions: Experimental and Numerical Aspects, Atmosphere-Ocean, 54(1), 60–74, doi:10.1080/07055900.2015.1119100, 2016b.

Asmi, E., Kondratyev, V., Brus, D., Laurila, T., Lihavainen, H., Backman, J., Vakkari, V., Aurela, M., Hatakka, J., Viisanen, Y., Uttal, T., Ivakhov, V. and Makshtas, A.: Aerosol size distribution seasonal characteristics measured in Tiksi, Russian Arctic, Atmos. Chem. Phys., 16(3), 1271–1287, doi:10.5194/acp-16-1271-2016, 2016.

Barrie, L. A.: Arctic air pollution: An overview of current knowledge, Atmos. Environ., 20(4), 643–663, doi:10.1016/0004-6981(86)90180-0, 1986.

Bigg, E. K. and Leck, C.: Properties of the aerosol over the central Arctic Ocean, J. Geophys. Res., 106(D23), 32101, doi:10.1029/1999JD901136, 2001.

Boé, J., Hall, A. and Qu, X.: September sea-ice cover in the Arctic Ocean projected to vanish by 2100, Nat. Geosci., 2(5), 341–343, doi:10.1038/ngeo467, 2009.

Brands, M., Kamphus, M., Böttger, T., Schneider, J., Drewnick, F., Roth, a., Curtius, J., Voigt, C., Borbon, a., Beekmann, M., Bourdon, a., Perrin, T. and Borrmann, S.: Characterization of a Newly Developed Aircraft-Based Laser Ablation Aerosol Mass Spectrometer (ALABAMA) and First Field Deployment in Urban Pollution Plumes over Paris During MEGAPOLI 2009, Aerosol Sci. Technol., 45(1), 46–64, doi:10.1080/02786826.2010.517813, 2011.

Brioude, J., Arnold, D., Stohl, A., Cassiani, M., Morton, D., Seibert, P., Angevine, W., Evan, S., Dingwell, A., Fast, J. D., Easter, R. C., Pisso, I., Burkhart, J. and Wotawa, G.: The Lagrangian particle dispersion model FLEXPART-WRF version 3.1, Geosci. Model Dev., 6(6), 1889–1904,

777 doi:10.5194/gmd-6-1889-2013, 2013.

778 Browse, J., Carslaw, K. S., Arnold, S. R., Pringle, K. and Boucher, O.: The scavenging processes
779 controlling the seasonal cycle in Arctic sulphate and black carbon aerosol, Atmos. Chem. Phys.,
780 12(15), 6775–6798, doi:10.5194/acp-12-6775-2012, 2012.

781 Browse, J., Carslaw, K. S., Mann, G. W., Birch, C. E., Arnold, S. R. and Leck, C.: The complex
782 response of Arctic aerosol to sea-ice retreat, Atmos. Chem. Phys., 14(14), 7543–7557,
783 doi:10.5194/acp-14-7543-2014, 2014.

784 Carslaw, K. S., Lee, L. A., Reddington, C. L., Pringle, K. J., Rap, A., Forster, P. M., Mann, G.
785 W., Spracklen, D. V, Woodhouse, M. T., Regayre, L. A. and Pierce, J. R.: Large contribution of
786 natural aerosols to uncertainty in indirect forcing., Nature, 503(7474), 67–71,
787 doi:10.1038/nature12674, 2013.

788 Chang, R. Y. W., Sjostedt, S. J., Pierce, J. R., Papakyriakou, T. N., Scarratt, M. G., Michaud, S.,
789 Levasseur, M., Leaitch, W. R. and Abbatt, J. P. D.: Relating atmospheric and oceanic DMS
790 levels to particle nucleation events in the Canadian Arctic, J. Geophys. Res. Atmos., 116(21), 1–
791 10, doi:10.1029/2011JD015926, 2011.

792 Charlson, R. J., Lovelock, J. E., Andreae, M. O. and Warren, S. G.: Oceanic phytoplankton,
793 atmospheric sulphur, cloud albedo and climate, Nature, 326, 655–661, doi:10.1038/326655a0,
794 1987.

795 Clarke, A. D., L, V. J., Eisele, F., Mauldin, R. L., Tanner, D. and M, L.: Particle production in
796 the remote marine atmosphere : Cloud outflow and subsidence during ACE 1, Earth Sci., 103,
797 1998.

798 Clarke, A. D., Kapustin, V. N., Eisele, F. L., Weber, R. J. , and McMurry, P. H.: Particle
799 production near marine clouds: sulfuric acid and predictions from classical binary nucleation,
800 Geophys. Res. Lett., 26, 2425-2428, doi: 10.1029/1999GL900438, 1999.

801 Covert, D. S., Wiedensohler, A., Aalto, P., Heintzenberg, J., McMurry, P. H. and Leck, C.:
802 Aerosol number size distributions from 3 to 500 nm diameter in the arctic marine boundary layer
803 during summer and autumn, Tellus, Ser. B Chem. Phys. Meteorol., 48(2), 197–212, 1996.

804 Croft, B., Martin, R. V., Leaitch, W. R., Tunved, P., Breider, T. J., D'Andrea, S. D. and Pierce, J.
805 R.: Processes controlling the seasonal cycle of Arctic aerosol number and size distributions,
806 Atmos. Chem. Phys., 16, 3665-3682, doi:10.5194/acp-16-3665-2016, 2016a.

807 Croft, B., G.R. Wentworth, R.V. Martin, W.R. Leaitch, J.G. Murphy, B.N. Murphy, J. Kodros,
808 J.P.D. Abbatt and J.R. Pierce. Contribution of Arctic seabird-colony ammonia to atmospheric
809 particles and cloud-albedo radiative effect. Nat. Commun. 7, 13444, doi: 10.1038/ncomms13444,
810 2016b.

811 DeCarlo, P. F., Kimmel, J. R., Trimborn, A., Northway, M. J., Jayne, J. T., Aiken, A. C., Gonin,
812 M., Fuhrer, K., Horvath, T., Docherty, K. S., Worsnop, D. R. and Jimenez, J. L.: Field-
813 deployable, high-resolution, time-of-flight aerosol mass spectrometer., Anal. Chem., 78(24),
814 8281–9, doi:10.1021/ac061249n, 2006.

815 Engvall, A.-C., Krecji, R., Sröm, J., Minikin, A., Treffeisen, R., Stohl, A. and Herber, A.: In-situ
816 airborne observations of the microphysical properties of the Arctic tropospheric aerosol during
817 late spring and summer, Tellus B, 0(0), 080414161623888–???, doi:10.1111/j.1600-
818 0889.2008.00348.x, 2008.

819 Engvall, a.-C., Krejci, R., Ström, J., Treffeisen, R., Scheele, R., Hermansen, O. and Paatero, J.:
820 Changes in aerosol properties during spring-summer period in the Arctic troposphere, Atmos.
821 Chem. Phys., 8, 445-462, doi:10.5194/acp-8-445-2008, 2008.

822 Garrett, T. J.: Effects of varying aerosol regimes on low-level Arctic stratus, Geophys. Res. Lett.,
823 31(17), L17105, doi:10.1029/2004GL019928, 2004.

824 Garrett, T. J., Hobbs, P. V and Radke, L. F.: High Aitken Nucleus Concentrations above Cloud
825 Tops in the Arctic, J. Atmos. Sci., 59(3), 779–783, doi:10.1175/1520-
826 0469(2001)059<0779:HANCAC>2.0.CO;2, 2002.

827 Garrett, T. J., Brattström, S., Sharma, S., Worthy, D. E. J. and Novelli, P.: The role of
828 scavenging in the seasonal transport of black carbon and sulfate to the Arctic, Geophys. Res.
829 Lett., 38(16), 1–6, doi:10.1029/2011GL048221, 2011.

830 Ge, X., Wexler, A. S. and Clegg, S. L.: Atmospheric amines - Part I. A review, Atmos. Environ.,
831 45(3), 524–546, doi:10.1016/j.atmosenv.2010.10.012, 2011.

832 Gibb, S. W., Mantoura, R. F. C. and Liss, P. S.: Ocean-atmosphere exchange and atmospheric
833 speciation of ammonia and methylamines in the region of the NW Arabian Sea, Global
834 Biogeochem. Cycles, 13(1), 161–178, doi:10.1029/98GB00743, 1999.

835 Hegg, D. A., Radke, L. F. and Hobbs, P. V: Particle production associated with marine clouds, J.
836 Geophys. Res. Atmos., 95(D9), 13917–13926, 1990.

837 Heintzenberg, B. J.: Particle size distribution and optical properties, Tellus, 32, 251–260,
838 10.1111/j.2153-3490.1980.tb00952.x, 1980.

839 Heintzenberg, B., Ström, J., Ogren, J. A., and Fimpel, H.-P.: Vertical profiles of aerosol
840 properties in the summer troposphere of central Europe, scandinavia and the svalbard region,
841 Atmos. Env., 25, 621-627, doi: 10.1016/0960-1686(91)90059-G, 1991.

842 Heintzenberg, B., and Leck, C.: Seasonal variation of the atmospheric aerosol near the top of the
843 marine boundary layer over Spitsbergen related to the Arctic sulphur cycle. Tellus B, 46, 52-67,
844 doi: 10.1034/j.1600-0889.1994.00005.x, 1994.

845 Heintzenberg, J., Leck, C., Birmili, W., Wehner, B., Tjernström, M., Wiedensohler, A.,
846 Tjernstrom, M. and Wiedensohler, A.: Aerosol number-size distributions during clear and fog
847 periods in the summer high Arctic: 1991, 1996 and 2001, Tellus B, 58(1), 41–50,
848 doi:10.1111/j.1600-0889.2005.00171.x, 2006.

849 Heintzenberg, J. and Leck, C.: The summer aerosol in the central Arctic 1991–2008: did it
850 change or not?, Atmos. Chem. Phys., 12(9), 3969–3983, doi:10.5194/acp-12-3969-2012, 2012.

851 Heintzenberg, J., Leck, C. and Tunved, P.: Potential source regions and processes of aerosol in
852 the summer Arctic, Atmos. Chem. Phys., 15(11), 6487–6502, doi:10.5194/acp-15-6487-2015,
853 2015.

854 Hoppel, W. a., Frick, G. M., Fitzgerald, J. W. and Larson, R. E.: Marine boundary layer
855 measurements of new particle formation and the effects nonprecipitating clouds have on aerosol
856 size distribution, J. Geophys. Res., 99(D7), 14443, doi:10.1029/94JD00797, 1994.

857 Karl, M., Leck, C., Gross, A. and Pirjola, L.: A study of new particle formation in the marine
858 boundary layer over the central Arctic Ocean using a flexible multicomponent aerosol dynamic

859 model, Tellus B, 64(0), 1–24, doi:10.3402/tellusb.v64i0.17158, 2012.

860 Karl, M., Leck, C., Coz, E. and Heintzenberg, J.: Marine nanogels as a source of atmospheric
861 nanoparticles in the high Arctic, Geophys. Res. Lett., 40(14), 3738–3743, doi:10.1002/grl.50661,
862 2013.

863 Kulmala, M., Dal Maso, M., Mäkelä, J. M., Pirjola, L., Väkevä, M., Aalto, P., Miikkulainen, P.,
864 Hämeri, K. and O'Dowd, C. D.: On the formation, growth and composition of nucleation mode
865 particles, Tellus, Ser. B Chem. Phys. Meteorol., 53, 479–490, doi:10.1034/j.1600-
866 0889.2001.d01-33.x, 2001.

867 Kupiszewski, P., Leck, C., Tjernström, M., Sjogren, S., Sedlar, J., Graus, M., M??ller, M.,
868 Brooks, B., Swietlicki, E., Norris, S. and Hansel, A.: Vertical profiling of aerosol particles and
869 trace gases over the central Arctic Ocean during summer, Atmos. Chem. Phys., 13(24), 12405–
870 12431, doi:10.5194/acp-13-12405-2013, 2013.

871 Law, K. S., Stohl, A., Quinn, P. K., Brock, C. A., Burkhart, J. F., Paris, J. D., Ancellet, G.,
872 Singh, H. B., Roiger, A., Schlager, H., Dibb, J., Jacob, D. J., Arnold, S. R., Pelon, J. and
873 Thomas, J. L.: Arctic air pollution: New insights from POLARCAT-IPY, Bull. Am. Meteorol.
874 Soc., 95(12), 1873–1895, doi:10.1175/BAMS-D-13-00017.1, 2014.

875 Leaitch, W.R., Hoff, R.M., Melnichuk, S., and Hogan, W.: Some chemical and physical
876 properties of the Arctic winter aerosol in northeastern Canada. J. Climate Appl. Meteorol., 23,
877 916-928, http://dx.doi.org/10.1175/1520-0450(1984)023<0916:SPACPO>2.0.CO;2, 1984.

878 Leaitch, W.R., Barrie, L.A., Bottenheim, J.W., Li, S.-M., Shepson, P. and Yokouchi, Y.:
879 Airborne observations related ozone depletion at polar sunrise. J. Geophys. Res., 99, 25499-
880 25517, 10.1029/94JD02750, 1994.

881 Leaitch, W. R., Sharma, S., Huang, L., Toom-Sauntry, D., Chivulescu, A., Macdonald, A. M.,
882 von Salzen, K., Pierce, J. R., Bertram, A. K., Schroder, J. C., Shantz, N. C., Chang, R. Y. W. and
883 Norman, A.-L.: Dimethyl sulfide control of the clean summertime Arctic aerosol and cloud,
884 Elem. Sci. Anth., 1(1), 17, doi:10.12952/journal.elementa.000017, 2013.

885 Leaitch, W. R., Korolev, A., Aliabadi, A. A., Burkart, J., Willis, M., Abbatt, J. P. D., Bozem, H.,
886 Hoor, P., Köllner, F., Schneider, J., Herber, A., Konrad, C. and Brauner, R.: Effects of 20-100

887 nanometre particles on liquid clouds in the clean summertime Arctic, Atmos. Chem. Phys., 16,
888 11107-11124, doi:10.5194/acp-16-11107-2016, 2016.

889 Leck, C. and Bigg, E. K.: Aerosol production over remote marine areas-A new route, Geophys.
890 Res. Lett., 26(23), 3577, doi:10.1029/1999GL010807, 1999.

891 Leck, C. and Bigg, E. K.: Source and evolution of the marine aerosol - A new perspective,
892 Geophys. Res. Lett., 32(19), 1–4, doi:10.1029/2005GL023651, 2005.

893 Leck, C. and Bigg, E. K.: New Particle Formation of Marine Biological Origin, Aerosol Sci.
894 Technol., 44(7), 570–577, doi:10.1080/02786826.2010.481222, 2010.

895 Lohmann, U. and Feichter, J.: Global indirect aerosol effects: a review, Atmos. Chem. Phys., 5,
896 715–735, doi:10.5194/acp-5-715-2005, 2005.

897 Mauldin, R. L., Madronich, S., Flocke, S. J. , Eisele, F. L. , Frost, G. J. and Prevot, A. S. H. :
898 New insights on OH: Measurements around and in clouds, Geophys. Res. Lett., 24(No 23),
899 3033-3036, doi:10.1029/97GL02983, 1997.

900 Mauritsen, T., Sedlar, J., Tjernström, M., Leck, C., Martin, M., Shupe, M., Sjogren, S., Sierau,
901 B., Persson, P. O. G., Brooks, I. M. and Swietlicki, E.: An Arctic CCN-limited cloud-aerosol
902 regime, Atmos. Chem. Phys., 11(1), 165–173, doi:10.5194/acp-11-165-2011, 2011.

903 Mungall, E. L., Croft, B., Lizotte, M., Thomas, J. L., Murphy, J. G., Levasseur, M., Martin, R.
904 V., Wentzell, J. J. B., Liggio, J. and Abbatt, J. P. D.: Dimethyl sulfide in the summertime Arctic
905 atmosphere: measurements and source sensitivity simulations, Atmos. Chem. Phys., 16(11),
906 6665–6680, doi:10.5194/acp-16-6665-2016, 2016.

907 Nguyen, Q. T., Glasius, M., Sørensen, L. L., Jensen, B., Skov, H., Birmili, W., Wiedensohler, A.,
908 Kristensson, A., Nøjgaard, J. K. and Massling, A.: Seasonal variation of atmospheric particle
909 number concentrations, new particle formation and atmospheric oxidation capacity at the high
910 Arctic site Villum Research Station, Station Nord, Atmos. Chem. Phys. Discuss., 1–41,
911 doi:10.5194/acp-2016-205, 2016.

912 Petters, M. D. and Kreidenweis, S. M.: A single parameter representation of hygroscopic growth
913 and cloud condensation nucleus activity, Atmos. Chem. Phys., 7, 1961–1971, 2007.

914 Pierce, J. R., Leaitch, W. R., Liggio, J., Westervelt, D. M., Wainwright, C. D., Abbatt, J. P. D.,
915 Ahlm, L., Al-Basheer, W., Cziczo, D. J., Hayden, K. L., Lee, A. K. Y., Li, S.-M., Russell, L. M.,
916 Sjostedt, S. J., Strawbridge, K. B., Travis, M., Vlasenko, A., Wentzell, J. J. B., Wiebe, H. A.,
917 Wong, J. P. S., and Macdonald, A. M.: Nucleation and condensational growth to CCN sizes
918 during a sustained pristine biogenic SOA event in a forested mountain valley, Atmos. Chem.
919 Phys., 12, 3147-3163, doi:10.5194/acp-12-3147-2012, 2012.

920 Pirjola, L., O'Dowd, C. D., Brooks, I. M. and Kulmala, M.: Can new particle formation occur in
921 the clean marine boundary layer?, J. Geophys. Res. Atmos., 105(D21), 26531–26546,
922 doi:10.1029/2000JD900310, 2000.

923 Quinn, P. K. and Bates, T. S.: The case against climate regulation via oceanic phytoplankton
924 sulphur emissions, Nature, 480(7375), 51–56, doi:10.1038/nature10580, 2011.

925 Quinn, P. K., Shaw, G., Andrews, E., Dutton, E. G., Ruoho-Airola, T. and Gong, S. L.: Arctic
926 haze: Current trends and knowledge gaps, Tellus, Ser. B Chem. Phys. Meteorol., 59(1), 99–114,
927 doi:10.1111/j.1600-0889.2006.00238.x, 2007.

928 Radke, F. L. and Hobbs, P. V.: Humidity and particle fields around some small cumulus clouds,
929 Journal of atmospheric sciences, 48(9), 1190-1193, doi: http://dx.doi.org/10.1175/1520-
930 0469(1991)048<1190:HAPFAS>2.0.CO;2, 1991.

931 Rahn, K. A., Borys, R. D. and Shaw, G. E.: The Asian source of Arctic haze bands, Nature, 268,
932 713-715, doi: 10.1038/268713a0, 1977.

933 Rehbein, P. J. G., Jeong, C. H., McGuire, M. L., Yao, X., Corbin, J. C. and Evans, G. J.: Cloud
934 and fog processing enhanced gas-to-particle partitioning of trimethylamine, Environ. Sci.
935 Technol., 45(10), 4346–4352, doi:10.1021/es1042113, 2011.

936 Riipinen, I., Pierce, J. R., Yli-Juuti, T., Nieminen, T., Häkkinen, S., Ehn, M., Junninen, H.,
937 Lehtipalo, K., Petäjä, T., Slowik, J., Chang, R., Shantz, N. C., Abbatt, J., Leaitch, W. R.,
938 Kerminen, V.-M., Worsnop, D. R., Pandis, S. N., Donahue, N. M., and Kulmala, M.: Organic
939 condensation: a vital link connecting aerosol formation to cloud condensation nuclei (CCN)
940 concentrations, Atmos. Chem. Phys., 11, 3865-3878, doi:10.5194/acp-11-3865-2011, 2011.

941 Seinfeld, J.H., and Pandis, S. N.: Atmospheric Chemistry and Physics: From Air Pollution to
942 Climate Change. 3rd Edition. John Wiley & Sons, Inc., 2016.

943 Shaw, G.E. and Stamnes, K.: Arctic haze: perturbations of the polar radiation budget. Ann. N. E
944 Ad. Aci. 338, 533-539, doi: 10.1111/j.1749-6632.1980.tb17145.x 1980.

945

946 Shaw, G. E.: The Arctic Haze Phenomenon, Bull. Am. Meteorol. Soc., 76, 2403–2413,
947 doi:10.1175/1520-0477(1995)076<2403:TAHP>2.0.CO;2, 1995.

948 Skamarock, W. C., Klemp, J. B., Dudhia, J., Gill, D. O., Barker, D. M., Wang, W. and Powers, J.
949 G.: A Description of the Advanced Research WRF Version 2, [online] Available from:
950 http://oai.dtic.mil/oai/oai?verb=getRecord&metadataPrefix=html&identifier=ADA487419
951 (Accessed 22 March 2016), 2005.

952 Sjostedt, S. J., Leaitch, W. R., Levasseur, M., Scarratt, M., Michaud, S., Motard-Côté, J.,
953 Burkhart, J. H., and Abbatt J.: Evidence for the uptake of atmospheric acetone and methanol by
954 the Arctic Ocean during late summer DMS-Emission plumes. J. Geophys. Res., 117, D12303,
955 doi: 10.1029/2011JD017086, 2012.

956 Stohl, a., Forster, C., Frank, A., Seibert, P. and Wotawa, G.: Technical note: The Lagrangian
957 particle dispersion model FLEXPART version 6.2, Atmos. Chem. Phys. Discuss., 5(4), 4739–
958 4799, doi:10.5194/acpd-5-4739-2005, 2005.

959 Ström, J., Umegård, J., Tørseth, K., Tunved, P., Hansson, H. C., Holmén, K., Wismann, V.,
960 Herber, A. and König-Langlo, G.: One year of particle size distribution and aerosol chemical
961 composition measurements at the Zeppelin Station, Svalbard, March 2000-March 2001, Phys.
962 Chem. Earth, 28(March 2000), 1181–1190, doi:10.1016/j.pce.2003.08.058, 2003.

963 Ström, J., Engvall, A. C., Delbart, F., Krejci, R. and Treffeisen, R.: On small particles in the
964 Arctic summer boundary layer: Observations at two different heights near Ny-Ålesund,
965 Svalbard, Tellus, Ser. B Chem. Phys. Meteorol., 61 B(2), 473–482, doi:10.1111/j.1600-
966 0889.2008.00412.x, 2009.

967 Tjernström, M., Birch, C. E., Brooks, I. M., Shupe, M. D., Persson, P. O. G., Sedlar, J.,

968 Mauritsen, T., Leck, C., Paatero, J., Szczodrak, M. and Wheeler, C. R.: Meteorological
969 conditions in the central Arctic summer during the Arctic Summer Cloud Ocean Study
970 (ASCOS), Atmos. Chem. Phys., 12(15), 6863–6889, doi:10.5194/acp-12-6863-2012, 2012.

971 Tjernström, M., Leck, C., Birch, C. E., Bottenheim, J. W., Brooks, B. J., Brooks, I. M., Bäcklin,
972 L., Chang, R. Y. W., De Leeuw, G., Di Liberto, L., De La Rosa, S., Granath, E., Graus, M.,
973 Hansel, a., Heintzenberg, J., Held, a., Hind, a., Johnston, P., Knulst, J., Martin, M., Matrai, P.
974 a., Mauritsen, T., Müller, M., Norris, S. J., Orellana, M. V., Orsini, D. a., Paatero, J., Persson, P.
975 O. G., Gao, Q., Rauschenberg, C., Ristovski, Z., Sedlar, J., Shupe, M. D., Sierau, B., Sirevaag,
976 a., Sjogren, S., Stetzer, O., Swietlicki, E., Szczodrak, M., Vaattovaara, P., Wahlberg, N.,
977 Westberg, M. and Wheeler, C. R.: The Arctic Summer Cloud Ocean Study (ASCOS): Overview
978 and experimental design, Atmos. Chem. Phys., 14(6), 2823–2869, doi:10.5194/acp-14-2823-
979 2014, 2014.

980 Tunved, P., Ström, J. and Krejci, R.: Arctic aerosol life cycle: linking aerosol size distributions
981 observed between 2000 and 2010 with air mass transport and precipitation at Zeppelin station,
982 Ny-Ålesund, Svalbard, Atmos. Chem. Phys., 13(7), 3643–3660, doi:10.5194/acp-13-3643-2013,
983 2013.

984 Twomey, S.: Pollution and the Planetary Albedo, Atmos. Environ., 41(Vol. 8), 1251–1256,
985 doi:10.1016/j.atmosenv.2007.10.062, 1974.

986 Wang, M. and Overland, J. E.: A sea ice free summer Arctic within 30 years: An update from
987 CMIP5 models, Geophys. Res. Lett., 39(17), 2–6, doi:10.1029/2012GL052868, 2012.

988 Weber, R. J., McMurry, P. H., Mauldin, L., Tanner, D. J., Eisele, F. L., Brechtel, F. J.,
989 Kreidenweis, S. M., Kok, G. L., Schillawski, R. D. and Baumgardner, D.: A study of new
990 particle formation and growth involving biogenic and trace gas species measured during ACE 1,
991 J. Geophys. Res., 103(D13), 16385–16396, doi:10.1029/97JD02465, 1998.

992 Wentworth, G. R., Murphy, J. G., Croft, B., Martin, R. V., Pierce, J. R., Côté, J.-S., Courchesne,
993 I., Tremblay, J.-É., Gagnon, J., Thomas, J. L., Sharma, S., Toom-Sauntry, D., Chivulescu, a.,
994 Levasseur, M. and Abbatt, J. P. D.: Ammonia in the summertime Arctic marine boundary layer:
995 sources, sinks and implications, Atmos. Chem. Phys., 16, 1937-1953, doi:10.5194/acp-16-1937-

2016, 2016.

Wiedensohler, A., Covert, D. S., Swietlicki, E., Aalto, P., Heintzenberg, J. and Leck, C.: Occurrence of an ultrafine particle mode less than 20 nm in diameter in the marine boundary layer during Arctic summer and autumn, Tellus, Ser. B Chem. Phys. Meteorol., 48(2), 213–222, doi:10.1034/j.1600-0889.1996.t01-1-00006.x, 1996.

Wiedensohler, A. H.-C. Hansson, D. Orsini, M. Wendisch, F. Wagner, K.N. Bower, T.W. Chourlarton, M. Wells, M. Parkin, K. Acker, W. Wieprecht, M.C. Facchini, J.A. Lind, S. Fuzzi, B.G. Arends, M. Kulmalao: Night-time formation and occurrence of new particles associated with orographic clouds, Atmos. Env., 31(16), 2445-2559, doi: http://dx.doi.org/10.1016/S1352-2310(96)00299-3, 1997.

Willis, M. D., Burkart, J., Thomas, J. L., Köllner, F., Schneider, J., Bozem, H., Hoor, P. M., Aliabadi, A. A., Schulz, H., Herber, A. B., Leaitch, W. R. and Abbatt, J. P. D.: Growth of nucleation mode particles in the summertime Arctic: a case study, Atmos. Chem. Phys., 7663–7679, doi:10.5194/acp-16-7663-2016, 2016.

Zhang, J., Spitz, Y. H., Steele, M., Ashjian, C., Campbell, R., Berline, L. and Matrai, P.: Modeling the impact of declining sea ice on the Arctic marine planktonic ecosystem, J. Geophys. Res. Ocean., 115(10), 1–24, doi:10.1029/2009JC005387, 2010.

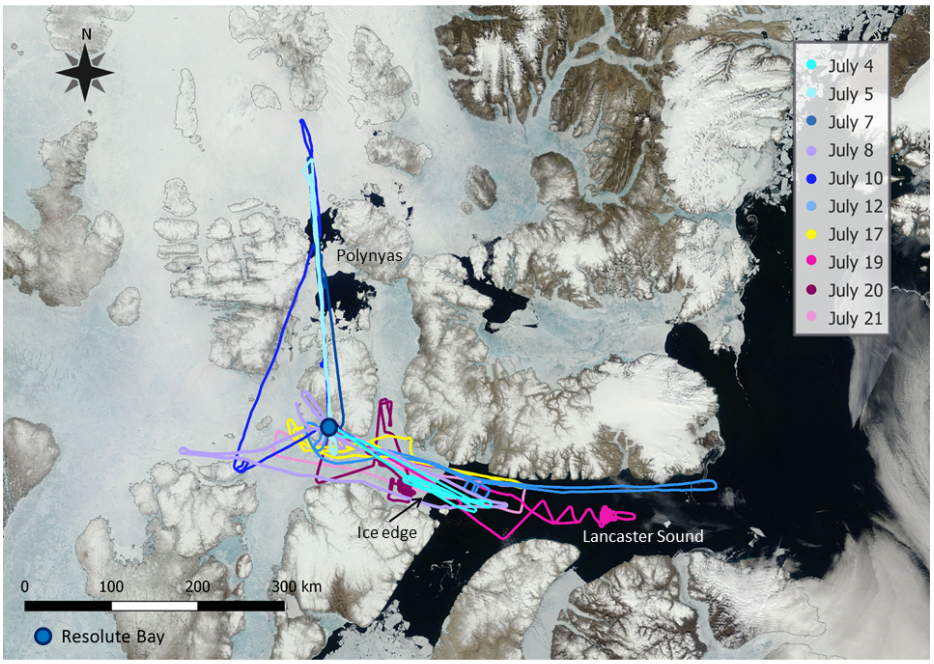

Figure 1. Compilation of all flight tracks plotted on a satellite image from July 4, 2014. The image is taken from: https://earthdata.nasa.gov/labs/worldview.

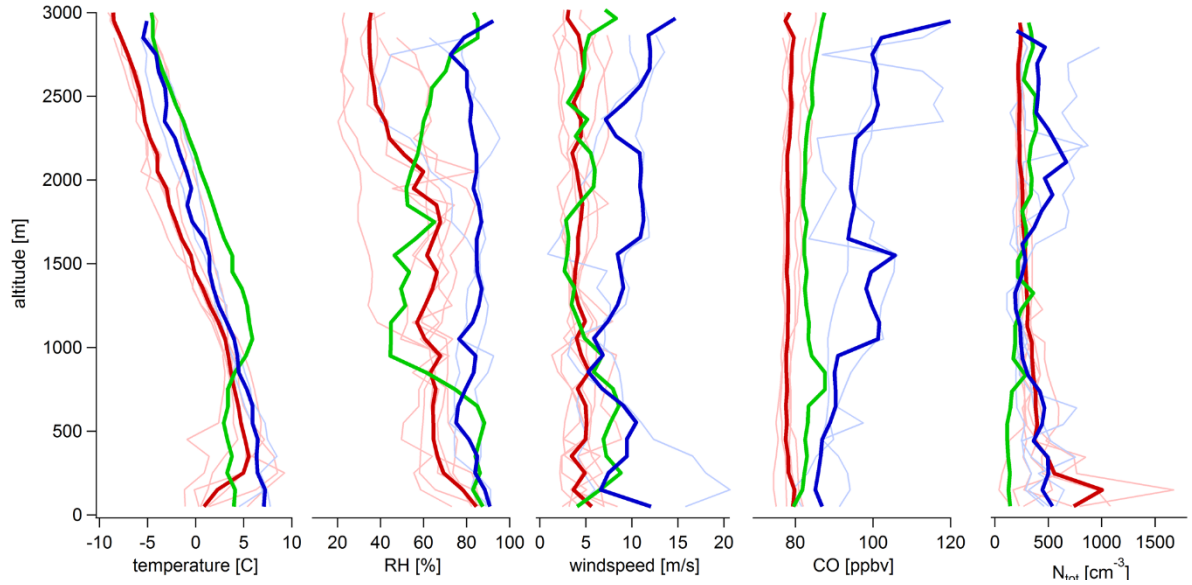

Figure 2. Median temperature, relative humidity (RH), wind speed,CO mixing ratio and N_{tot} profiles for the Arctic air mass period (dark red), the transition day (dark green), and the southern air mass period (dark blue). Median profiles for each flight are plotted in the background in the corresponding light colours.

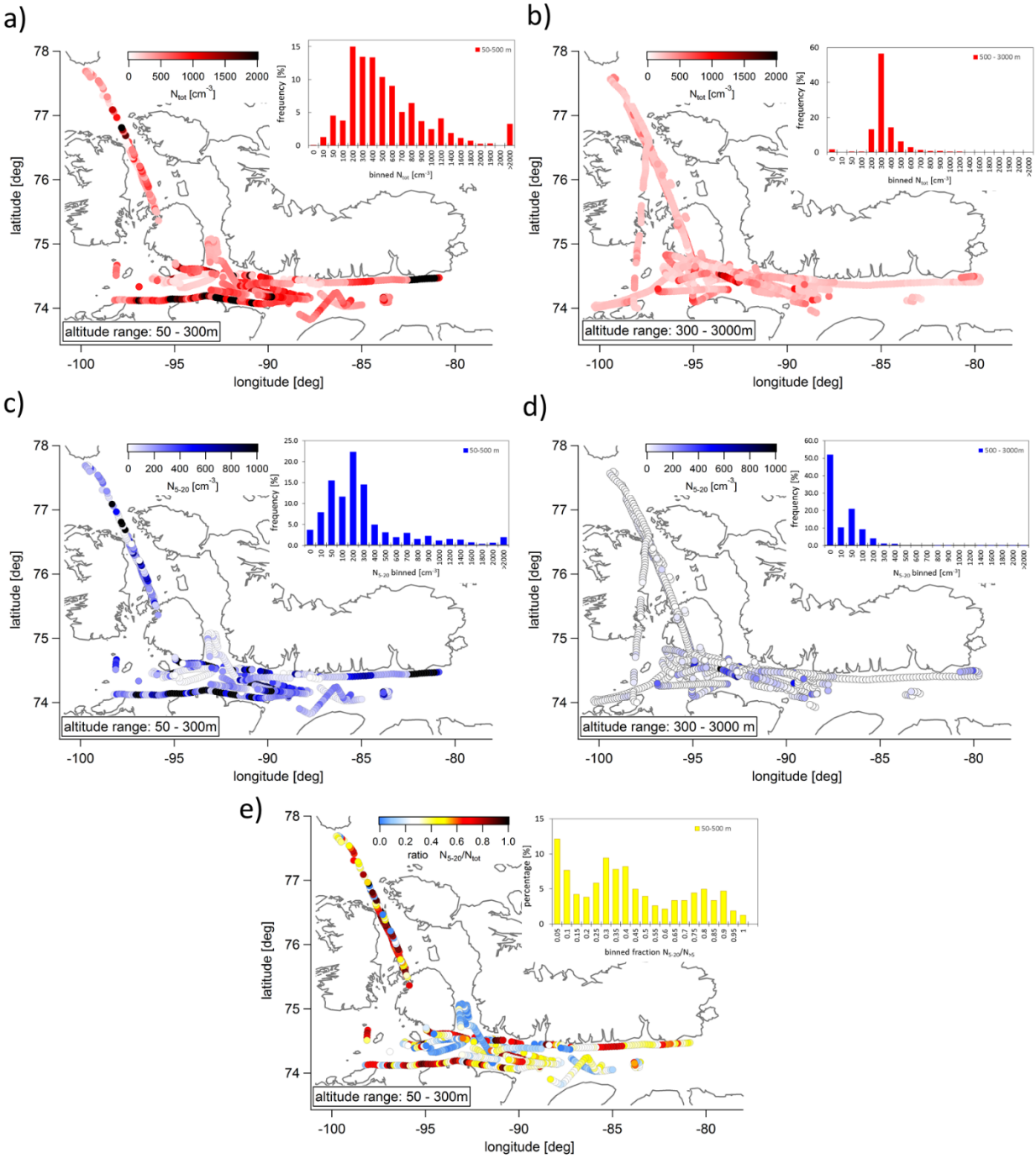

Figure 3. Flight tracks colour coded by particle concentrations. a.) Flight tracks within the boundary layer (50-300 m) colour coded by N_{tot}. b) Flight tracks within the free troposphere (300-3000 m) colour coded by N_{tot}. c) Flight tracks within the boundary layer (50-300m) colour

coded by UFP. d) Flight tracks within the free troposphere (300-3000 m) colour coded by $N_{5\text{-}20}$. e) Flight tracks within the boundary layer (50-300 m) colour coded by the ratio of $N_{5\text{-}20}/N_{tot}$

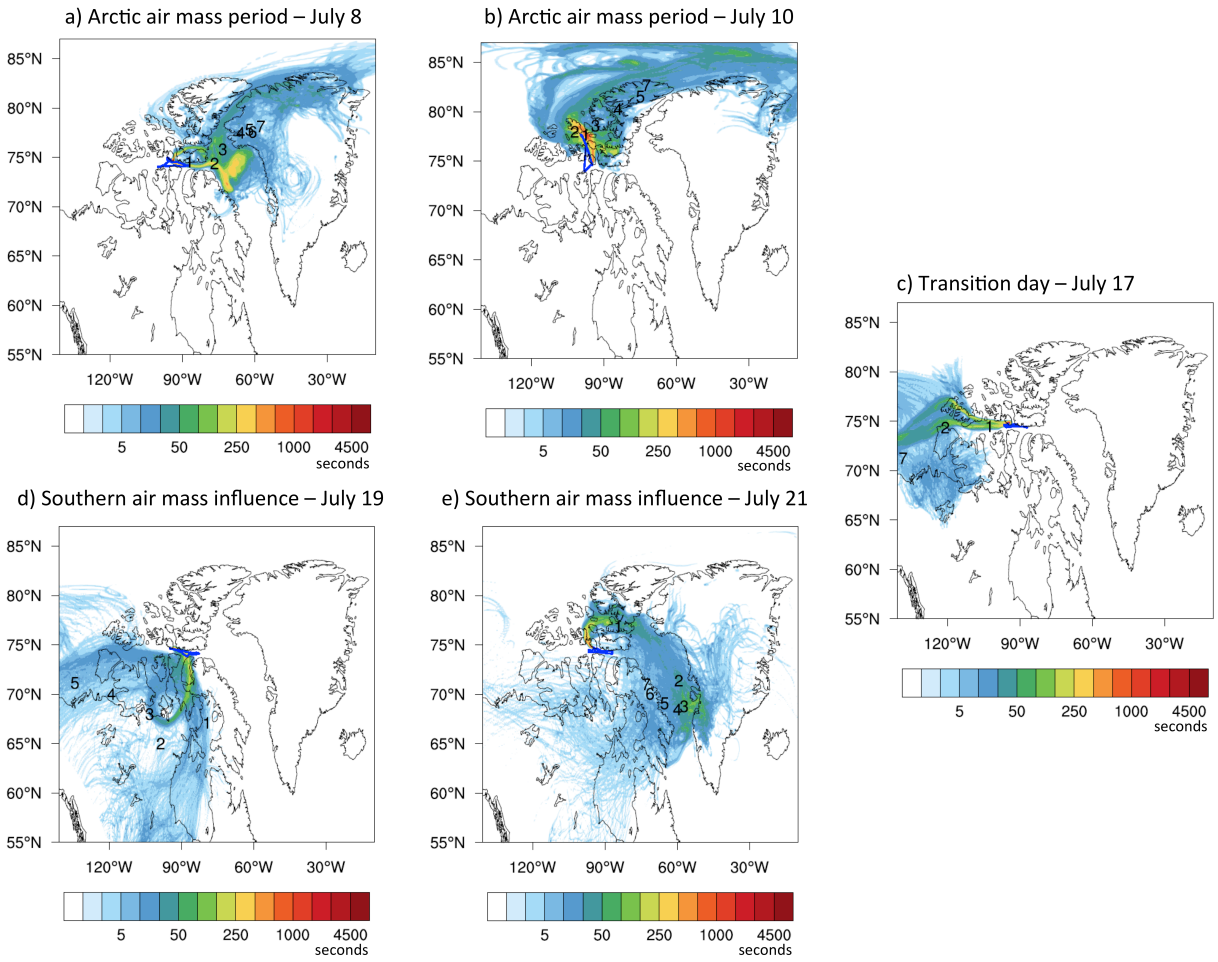

Figure 4. FLEXPART-WRF potential emissions sensitivities for each flight (using particle releases every 2 minutes along the flight track) that illustrate transport regimes during different periods of the campaign. The colour code indicates the residence time of air in seconds and the numbers represent the position of the plume centroid location in days prior to release (days 1-7).

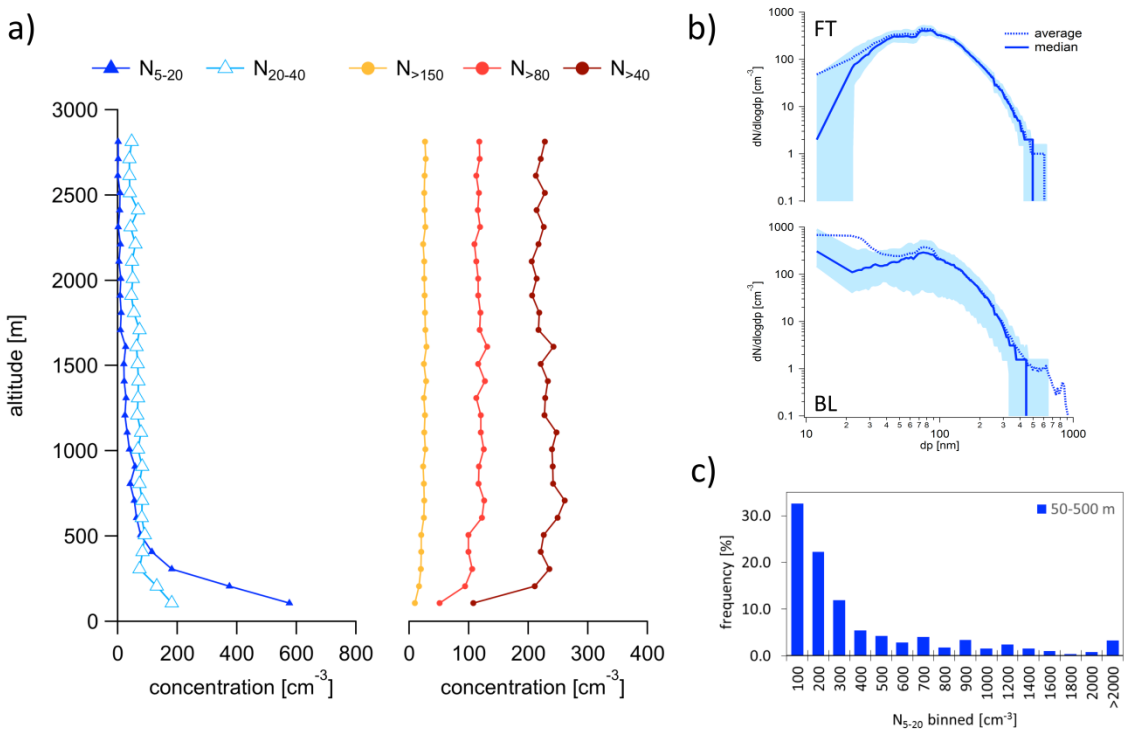

1041

1042 Figure 5. Average particle concentration data during the Arctic air mass period. a) Average
1043 vertical profiles of $N_{5\text{-}20}$, $N_{20\text{-}40}$, $N_{>40}$, $N_{>80}$, and $N_{>150}$. b) Average (solid line) and median
1044 (dashed line) size distribution within the BL and the FT. The light blue area represents the 25-
1045 75th % percentile range. c) Frequency distribution of the occurrence of UFP illustrates the large
1046 variability of the UFP concentrations within the BL.

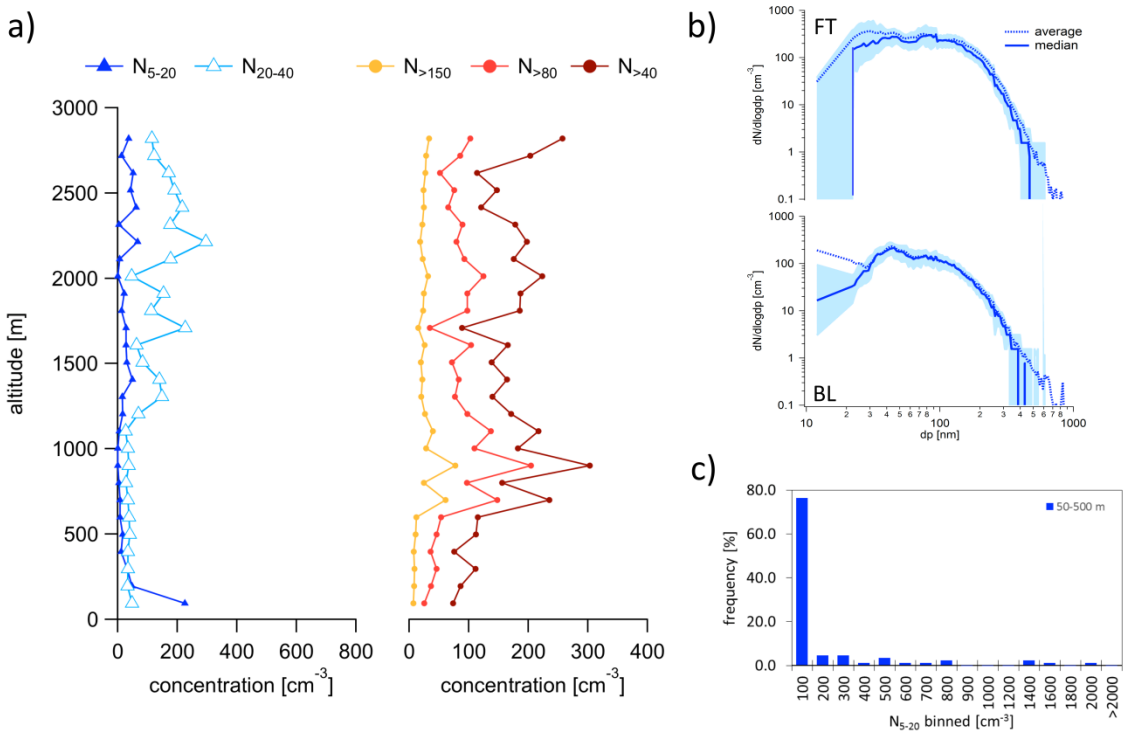

Figure 6. Average particle concentration data on the transition day. a) Average vertical profiles of $N_{5\text{-}20}$, $N_{20\text{-}40}$, $N_{>40}$, $N_{>80}$, and $N_{>150}$. b) Average (solid line) and median (dashed line) size distribution within the BL and the FT. The light blue area represents the 25-75th % percentile range. c) Frequency distribution of the occurrence of UFP illustrates the large variability of the UFP concentrations within the BL.

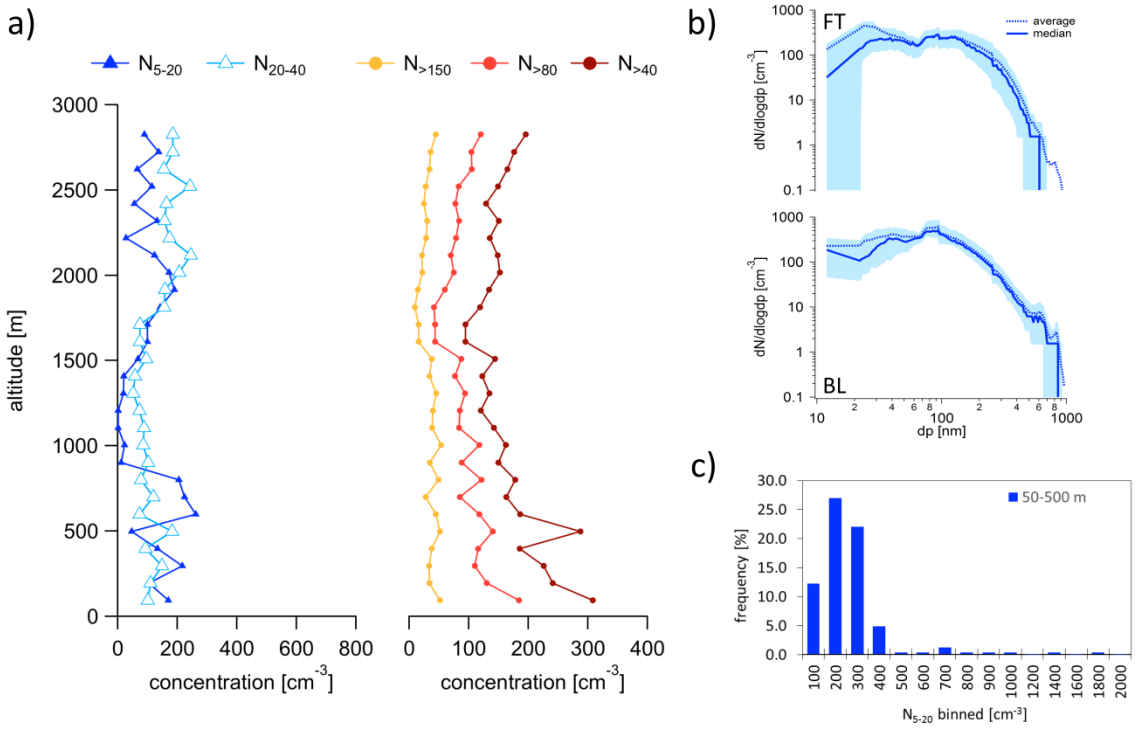

Figure 7. Average particle concentration data during the southern air mass period. a) Average vertical profiles of $N_{5\text{-}20}$, $N_{20\text{-}40}$, $N_{>40}$, $N_{>80}$, and $N_{>150}$. b) Average (solid line) and median (dashed line) size distribution within the BL and the FT. The light blue area represents the 25-75th % percentile range. c) Frequency distribution of the occurrence of UFP illustrates the large variability of the UFP concentrations within the BL.

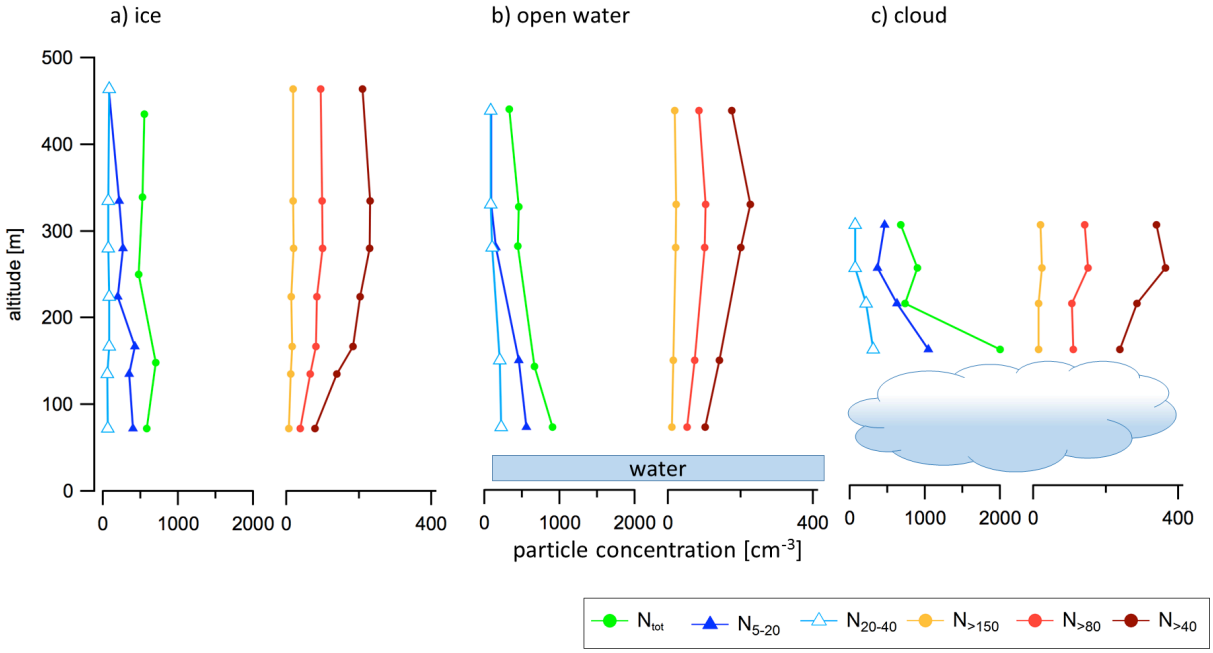

Figure 8. Average profiles of particle concentrations above ice, open water and cloud. The number of data points for each specific profile is: 130 above water, 216 above cloud, and 123 above water.

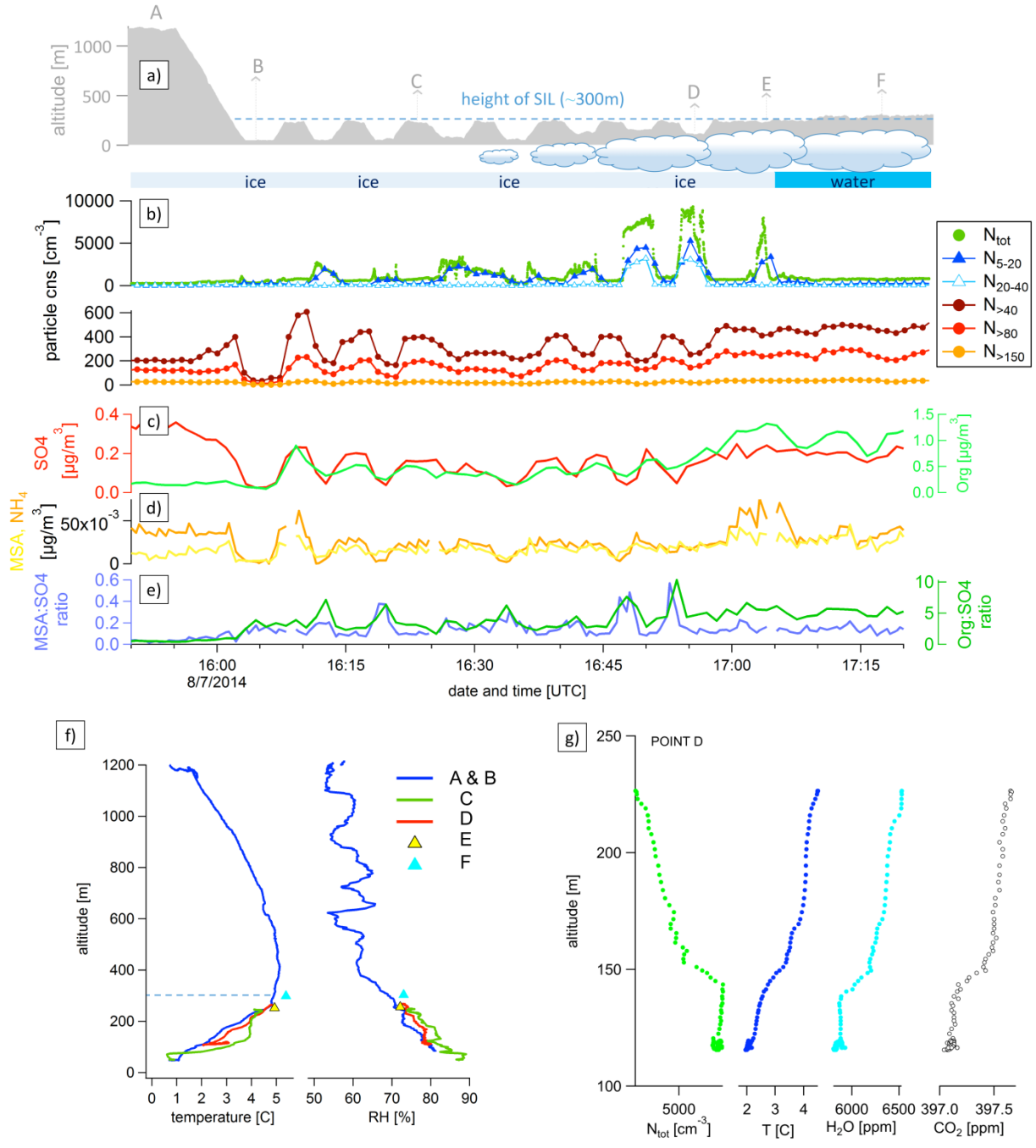

Figure 9. Case study from July 8 flight. Time series of flight altitude and illustration of the surface including cloud coverage (a), aerosol size (b) and chemical composition (c-e). (f)

1072 Vertical profiles of temperature and RH at locations A-F. (g) N_{tot}, temperature, H_2O mixing ratio
1073 and CO_2 profiles at location D.

1074

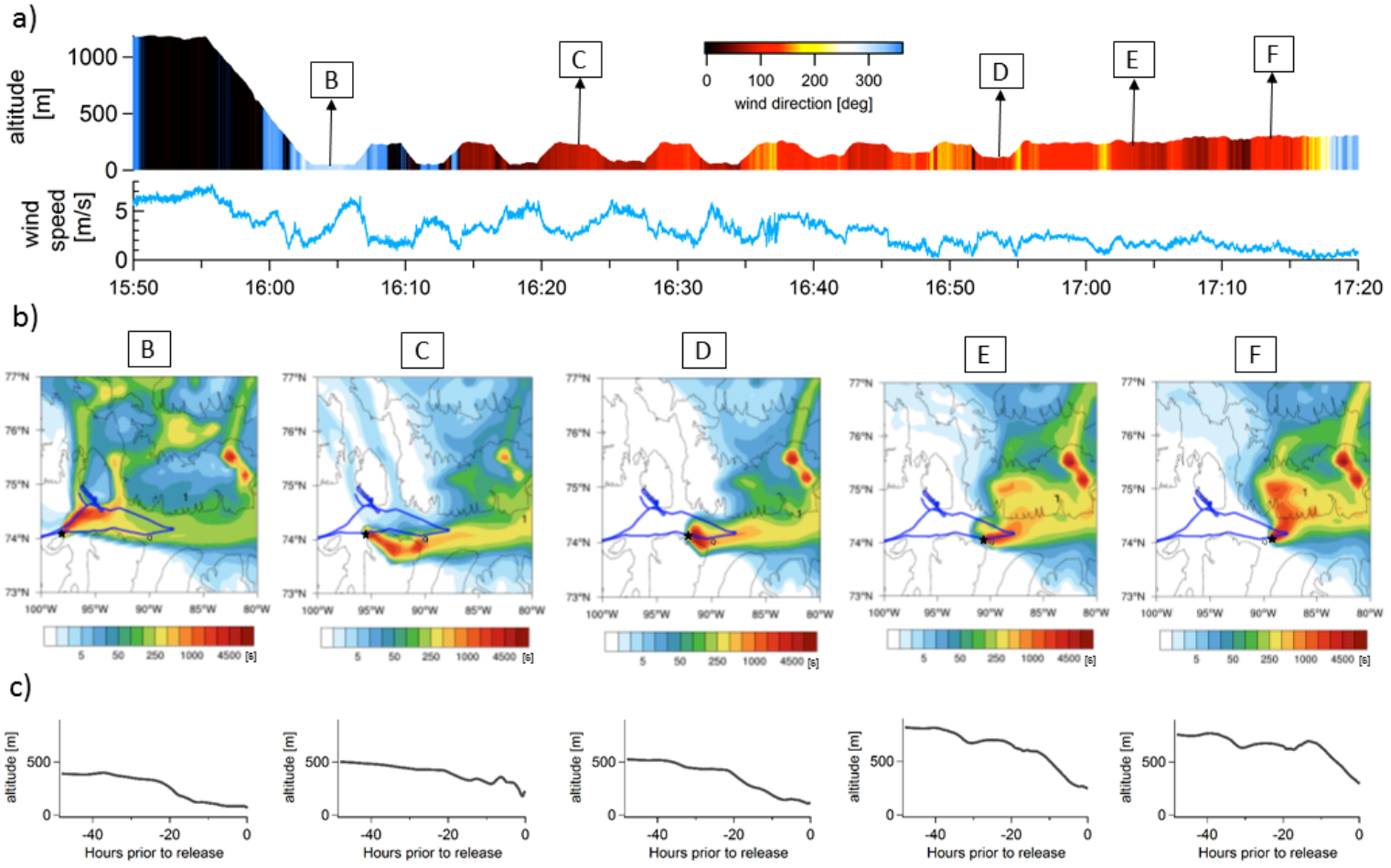

1075

1076

Figure 10. (a) Time series of aircraft altitude color coded with the wind direction and time series of wind speed (b) FLEXPART-WRF seven day backwards potential emissions sensitivities for points along the flight track (60 second release at time at indicated time and location) showing the air mass history at 5 representative locations within the SIL. The plume centroid location for particles with age of one day is indicated. (c) The bottom plots show the altitude of plume centroid 48 hours back in time.

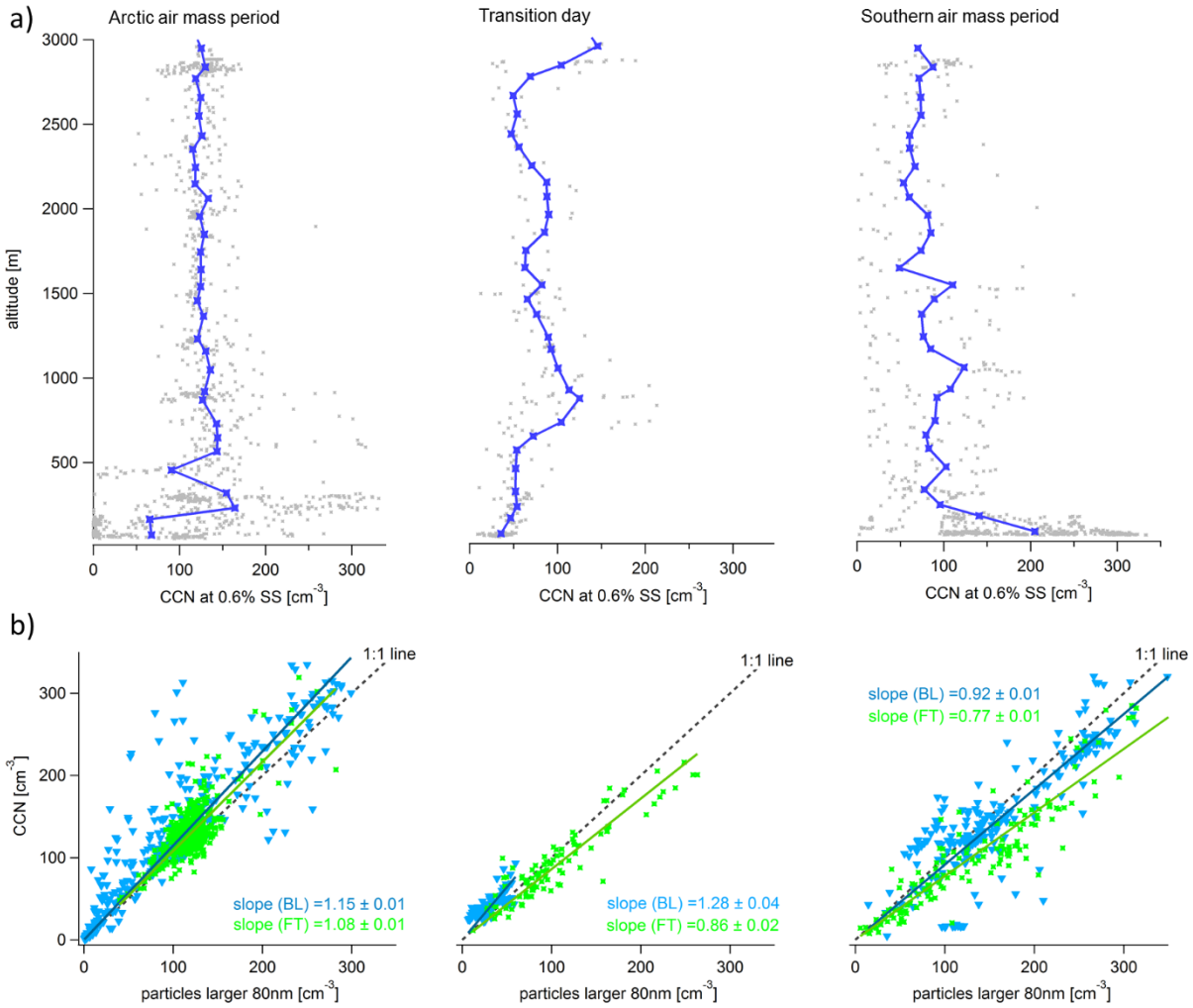

Figure 11. (a) Vertical profiles of average CCN concentrations (dark blue). All data points are plotted in light grey. (b) Correlation plots between CCN concentrations and particles larger than 80nm.

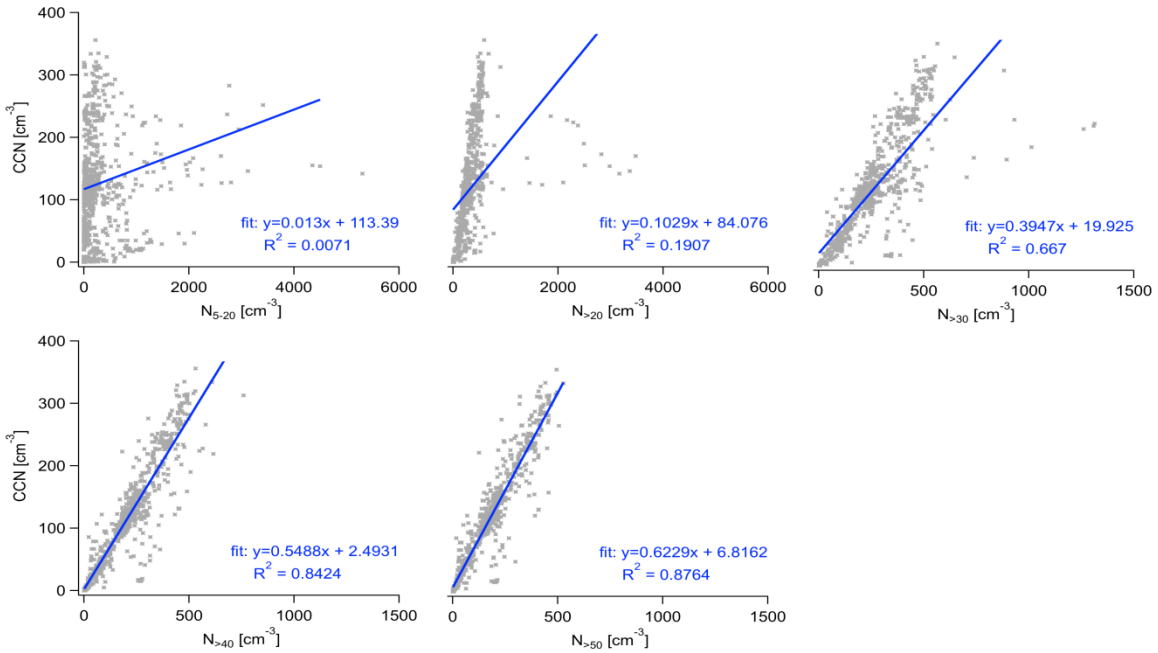

Figure 12. Correlations between CCN and particle concentrations for the full study period.